Appraising GDGT-based seawater temperature indices in the Southern Ocean

S. Fietz[a†*], S.L. Ho[b†,1], C. Huguet[c], A. Rosell-Melé[c,d], A. Martínez-García[e]

[a]*Department of Earth Sciences, Stellenbosch University, Stellenbosch, South Africa*

[b]*Alfred Wegener Institute, Helmholtz Centre for Polar and Marine Research, Potsdam, Germany*

[c]*Institut de Ciència i Tecnologia Ambientals, Universitat Autònoma de Barcelona, Bellaterra, Catalonia, Spain*

[d]*Institució Catalana de Recerca i Estudis Avançats, Barcelona, Catalonia, Spain*

[e]*Geological Institute, Swiss Federal Institute of Technology Zürich, Zürich, Switzerland*

[†]These authors contributed equally to the study.

*Corresponding author: *E-mail* address s_fietz@web.de (S. Fietz).

[1.]Present address: Bjerknes Centre for Climate Research and University of Bergen, Allegaten 41, 5007 Bergen, Norway.

ABSTRACT

A robust understanding of past oceanographic variability in the Southern Ocean is important because of its role in modulating global climate change. Here we analyzed the distributions of isoprenoid glycerol dialkyl glycerol tetraethers (GDGTs), both non-hydroxylated and the more recently discovered hydroxylated ones, in a well studied 500 kyr sediment record (core PS2489-2) from the Atlantic sector of the Southern Ocean and reconstructed past sea surface temperature. Given the uncertainty in the GDGT temperature indices, we appraised existing calibrations by comparing them with other temperature proxies and cold-water mass indicators determined from the same core. None of the existing calibrations afforded temporal trends and/or absolute values consistent with other better constrained temperature proxies. Using an extended compilation from a global core top hydroxylated GDGT data set, we examined if the disagreement might stem from the calibration data set and the definition of the GDGT indices. Among the new GDGT indices tested, the OH^{C} index (an extended TEX_{86} index modified similarly to the U^{K}_{37} index) and OH^{L} (including a log function similar to TEX_{86}^{L}) showed temporal variability that was the most consistent with other proxies. However, they also gave unrealistic sub-zero glacial temperature values, which may have been caused by a biased calibration due to the small calibration data set, and/or a shift in production or export depth of GDGTs during glacial stages which, in turn, result in a GDGT-temperature relationship different from that during the interglacial stages.

35 **Keywords**

36 Paleothermometry

37 Hydroxylated isoprenoid glycerol dialkyl glycerol tetraethers

38 OH-GDGTs

39 TEX_{86}

40 Cores PS2489-2/ODP1090

1. Introduction

Knowledge of sea surface temperature (SST) values helps us to understand oceanic heat transport and climate sensitivity to natural forcing; therefore, accurate estimates of past SSTs are of paramount importance. Biogeochemical proxies capture information on the growth environment of the source organisms, so are routinely used to infer past climate beyond the instrumental era. Various biogeochemical SST proxies are applied to marine sedimentary archives, including those derived from glycerol dialkyl glycerol tetraethers (GDGTs). The latter are cell membrane lipids synthesized by the Archaea and some bacteria, and are found in most environments on Earth (see Schouten et al., 2013, for a review). Isoprenoid (iso-)GDGTs are biosynthesized mainly by Thaumarchaeota, which are ubiquitous in the global ocean (see Schouten et al., 2013, for a review), and arguably by planktonic Euryarchaeota (Lincoln et al., 2014a,b; Schouten et al. 2014). Variations in the molecular structure of isoGDGTs, i.e. the number of cyclopentane moieties, are thought to be an adaptation to growth temperature, so, the relative distribution of isoGDGTs was proposed as a proxy for SST through the TEX_{86} index (Schouten et al., 2002). Kim et al. (2008) established a global TEX_{86}-SST calibration based on 287 marine sediment core tops, which has been applied in many climate reconstruction studies from the tropics to the poles (see Schouten et al., 2013, for a review).

However, Kim et al. (2008) also found that the relationship between core top TEX_{86} values and overlying satellite SST was non-linear below 5 °C. Subsequent studies of core tops from polar regions by Kim et al. (2010) revealed a considerable scatter in the TEX_{86} to SST relationship, prompting the proposal of a modified index, termed TEX_{86}^{L}, for application at subpolar sites (overlying SST < 15 °C). Subsequently, Ho et al. (2014) found that TEX_{86} and TEX_{86}^{L} values for surface sediments from the Southern Ocean and the North Pacific do usually covary with overlying SST and suggested that the isoGDGT paleothermometry might

66 be a suitable tool for paleotemperature reconstruction in these subpolar regions. An exception
67 would be the application of TEX_{86} proxies in the vicinity of Siberian river mouths and sea ice
68 margins, or sites with a potentially substantial contribution from methanogenic and/or
69 methanotrophic Archaea. Nonetheless, both Kim et al. (2010) and Ho et al. (2014) found
70 considerable scatter in the TEX_{86} and TEX_{86}^{L} vs. SST correlations, which led to a large
71 uncertainty in the estimated paleotemperature values.

72 Recently, structurally different GDGTs, i.e. isoprenoid hydroxylated GDGTs (OH-GDGTs),
73 which biosynthetically could originate from both Euryarchaeota and Thaumarchaeota, were
74 reported to occur widely in marine surface sediments (Liu et al., 2012a). OH-GDGTs occur
75 in low abundance in low latitude or warm water. For instance, only 1% relative to the total
76 isoGDGTs had been found in the tropical North Pacific (Xie et al., 2014) and up to 8% in
77 tropical and temperate regions (Liu et al., 2012a). A higher abundance was observed in high
78 latitude or cold water (Huguet et al., 2013). A study, combining water column particulate
79 matter and sedimentary material, has suggested that the contribution of OH-GDGTs to the
80 total isoGDGT pool (%OH) could be used as a new paleothermometer (Huguet et al., 2013).
81 Fietz et al. (2013) observed that %OH and changes in the OH-GDGT cyclopentane moieties
82 in the water column and core top samples were related to the influence of cold water masses
83 in the Fram Strait (Atlantic Arctic). Fietz et al. (2013) also observed that along a 42 cm
84 sediment core section spanning ca. the past 2000 years from the Atlantic Arctic, both %OH
85 and changes in the OH-GDGTs cyclopentane moieties correlated significantly with the
86 percentage contribution of the $C_{37:4}$ alkenone to the total C_{37} alkenone pool ($\%C_{37:4}$), an
87 indicator of cold polar water (Rosell-Melé, 1998). The TEX_{86} and TEX_{86}^{L} indices, in
88 contrast, provided unrealistic temporal changes and SST estimates for the Fram Strait core
89 (Fietz et al., 2013). SST changes derived from %OH also corroborated the historic Arctic sea-
90 ice development obtained from the molecular sea-ice indicator, IP_{25} (Knies et al., 2014).

TEX_{86} and TEX_{86}^{L} were used to study Holocene temperature changes in the Southern Ocean (e.g. Shevenell et al., 2011; Kim et al., 2012; Etourneau et al., 2013), as well as temperature variability during marine isotope stage 5 (MIS 5; Hayes et al., 2014). Here we tested the applicability of isoprenoid hydroxylated and non-hydroxylated GDGT-based indices to reconstruct paleotemperature values over five glacial-interglacial (G-IG) cycles at site PS2489-2 in the subantarctic Atlantic. The downcore applicability of the indices over G-IG cycles was assessed from their fit with published proxy records (e.g. Becquey and Gersonde, 2003; Martínez-García et al., 2009).

2. Methods

2.1. Site locations

Our compilation contains 52 surface sediment samples (Fig, 1A; Supplementary information Table S1) from three sample batches: (i) tropical - temperate from our archives (details given by Huguet et al., 2013), (ii) Arctic Ocean collected during R/V Polarstern expedition ARK-XXIII/1 (Huguet et al., 2013) and (iii) Pacific Southern Ocean collected during R/V Polarstern voyage ANT-XXVI/2 (as described by Ho et al., 2014). While both iso- and OH-GDGT data were used by Huguet et al. (2013), only isoGDGTs were reported by Ho et al. (2014), so OH-GDGTs are added here. We used only samples whereby all nine iso- and OH-GDGTs were detected to prevent bias in the statistical analysis due to analytical errors associated with samples with low GDGT abundance. For instance, GDGT-5' (crenarchaeol regiosomer) and/or OH-GDGT-2 were below detection limit in the core top samples from the Fram Strait described by Fietz et al. (2013) and were therefore not included in our compilation.

Core PS2489-2 (42°52.40'S, 8°58.40'E; Fig. 1A) was recovered from the Subantarctic Atlantic at 3794 m water depth. It was subsampled from surface to 1146 cm core depth, corresponding to 0 to 500 kyr at a resolution of 1–5 kyr (Martínez-García et al., 2009). PS2489-2 and neighbouring ODP Site 1090 (42°54.80'S, 8°53.90'E) samples had been previously analysed for a range of environmental proxies and spliced together, as described by Martínez-García et al. (2009, 2010, 2014). The initial age model for PS2489-2 was generated by Becquey and Gersonde (2002) and was revised by Martínez-García et al. (2009). Here we used the revised age model. Crenarchaeol concentration data for this core were given by Fietz et al. (2011a,b). Details of iso- and OH-GDGT composition in PS2489-2 are presented in this study.

Modern annual mean temperature derived from World Ocean Atlas 09 (WOA09; Locarnini et al., 2010) at 42.5°S, 8.5°E is 10.1 °C at the surface (0 m), 8.1 °C at 200 m and 3.0 °C at 1000 m (Fig. 1B). At the sea surface (0 m), summer (Jan. - March) average is slightly warmer with 10.9 °C and winter (July – September) average is slightly cooler with 9.2 °C (Fig. 1C). Warmest atlas SST values are recorded for March, with 11.2 °C, and lowest for September, with 8.9 °C.

2.2. GDGT analysis

Methodological details of GDGT extraction and separation are given by Huguet et al. (2013) for all tropical-temperate and Arctic surface sediments, by Ho et al. (2014) for Pacific Southern Ocean surface sediments and by Fietz et al. (2011a,b) for core PS2489-2 samples. In brief, freeze dried material was microwave extracted with dichloromethane (DCM):MeOH (3/1, vol/vol). The temperature in the extraction vessels of the microwave was increased to 70 °C. Different fractionation protocols were used for different samples; for instance, PS2489-2 extracts were analyzed without further fractionation (Fietz et al., 2011a,b), while surface

sediments from the temperate-tropical regions were manually divided into apolar and polar fractions using activated silica gel or activated alumina and sequentially eluted with mixtures of hexane:DCM and DCM:MeOH as eluents (Huguet et al., 2013). For the Arctic (Huguet et al., 2013) and the Pacific Southern Ocean (Ho et al., 2014) samples, a high performance liquid chromatography (HPLC) system equipped with a LiChrospher silicon dioxide column was used for the separation of apolar and polar fractions from the total extracts. All filtered extracts (core tops and PS2489-2 samples) were examined using HPLC-mass spectrometry with atmospheric pressure chemical ionization (LC-APCI-MS) equipped with a Tracer Excel Cyano column.

Detection of iso- and OH-GDGTs was done in single ion monitoring (SIM) mode of $[M+H]^+$ ± 0.5 m/z. Target compounds were GDGT-0 (*m/z* 1302), GDGT-1 (*m/z* 1300), GDGT-2 (*m/z* 1298), GDGT-3 (*m/z* 1296), and crenarchaeol and its regioisomer (*m/z* 1292) for non-hydroxylated isoGDGTs. OH-GDGTs are detectable with the same SIM scans as the isoGDGTs since, under APCI conditions, the OH-GDGTs easily dehydrated to give $[M+H-18]^+$ (Liu et al., 2012a,b). Hence OH-GDGT-0, for instance, with *m/z* at 1318 is detectable at *m/z* 1300. OH-GDGTs were determined at *m/z* 1300 (OH-GDGT-0), *m/z* 1298 (OH-GDGT-1) and *m/z* 1296 (OH-GDGT-2). Examples of OH-GDGT relative retention times (i.e. later elution in our LC-MS system) are given by Huguet et al. (2013) and Fietz et al. (2013).The structures of OH-GDGTs are described in detail by Liu et al. (2012a,b). The assignment of the OH-GDGTs using our routine analytical system is described in detail by Huguet et al. (2013) and Fietz et al. (2013). OH-GDGT assignment for the Pacific Southern Ocean surface sediments and in core PS2489-2 was carried out identically. Briefly, the OH-GDGT assignment was based on (i) fragmentation patterns consistent with isoGDGTs as shown by Hopmans et al. (2000), (ii) relative retention times between GDGT-0, crenarchaeol, branched GDGTs and OH-GDGTs consistent with those described by Liu et al. (2012b), (iii) exact

masses of the relevant peaks analysed from a sediment from the Fram Strait matching the theoretical masses for OH-GDGTs. The term "isoGDGTs" refers below to the non-hydroxylated isoprenoid GDGTs and the term "OH-GDGTs" to the hydroxylated isoprenoid GDGTs. The term "isoprenoid GDGTs" includes both types, though, so refers to the sum of isoGDGTs plus the sum of OH-GDGTs.

2.3. GDGT-based indices

TEX_{86} and TEX_{86}^{L} indices were calculated according to Schouten et al. (2002) and Kim et al. (2010), respectively. SST estimates were calculated using the TEX_{86} and TEX_{86}^{L} calibrations from Kim et al. (2010). Further information on the accuracy and reproducibility of TEX_{86} and TEX_{86}^{L} measurements is given by Fietz et al. (2013; online Supplementary material). The %OH index was calculated according to Huguet et al. (2013):

$$\%OH = (\Sigma OH\text{-}GDGTs)/(\Sigma OH\text{-}GDGTs+\Sigma isoGDGTs)*100. \quad (1)$$

Huguet et al. (2013) proposed a global OH-GDGT-based SST calibration ($SST_{\%OH\ global}$) based on surface sediment samples:

$$SST_{\%OH\ global} = (\%OH - 8.3)/(-0.24). \quad (2)$$

Fietz et al. (2013) presented an additional regional calibration based on core tops from the Arctic ($SST_{\%OH\ Arctic}$):

$$SST_{\%OH\ Arctic} = (\%OH - 8.6)/(-0.67). \quad (3)$$

Upon finding that existing GDGT-based calibrations produce unrealistic temperature variations relative to other temperature proxies (Section 3.2), we carried out regression analysis on a new compilation of core top OH-GDGT data (Table S1) to examine if there was an index that correlated better with temperature. We adopted the empirical approach of Kim et al. (2010), whereby all possible combinations of GDGTs from a pre-defined GDGT pool

are regressed against atlas SST and the combination giving the strongest correlation with SST is chosen as the temperature index. Following this approach, we tested the GDGT combinations of two GDGT pools defined as:

(a) Pool 1 (210 combinations), consisting of all TEX_{86} GDGTs, i.e. GDGT-1, GDGT-2, GDGT-3 and crenarchaeol regioisomer.

(b) Pool 2 (16002 combinations), consisting of all TEX_{86} GDGTs and all OH-GDGTs, i.e. GDGT-1, GDGT-2, GDGT-3, crenarchaeol regioisomer, OH-GDGT-0, OH-GDGT-1 and OH-GDGT-2.

3. Results and discussion

3.1. G-IG changes in GDGT distributions and temperature proxies

The G-IG oscillation in OH-GDGT abundance throughout the past 500 kyr mirrored that of other biomarkers, including isoGDGTs, alkenones and chlorins, the latter reflecting overall phytoplankton productivity (Harris et al., 1996), with higher abundance during glacial stages (Fig. 2). Despite the general similarity in increased GDGT abundance during glacial periods, the relative abundance of OH-GDGTs to isoGDGTs, the %OH index (Section 2.3), also showed G-IG cycles, with higher relative abundances during glacial stages (Fig. 2F). The relative abundances of GDGT-0, -1, -2 and crenarchaeol (GDGT-5) correlated significantly with SST derived from U^{K}_{37} for PS2489-2 (SST_{UK37}; Martínez-García et al., 2009), while OH-GDGT-0 and -1 showed significant negative correlations (Table 1; Supplementary material Fig. S1A). Comparison with SST_{UK37} was chosen over comparison with summer temperature derived from foraminifera ($SSST_{foram}$; Becquey and Gersonde, 2003) to allow a direct proxy comparison since both GDGTs and alkenones in the same samples were analysed, while foraminifera in different sediment depth sections were analysed.

The resulting glacial %OH increase (Fig. 2F) is consistent with the glacial decrease in SST values inferred from alkenones and foraminifera (Fig. 3A,B), the deuterium derived temperature evolution in Antarctica (Fig. 3C; Jouzel et al., 2007), as well as the glacial increase in proxy records of cold water mass indicators such as $\%C_{37:4}$ (Fig. 3D; Martínez-García et al. (2010)), and the relative distribution of the left-coiling *Neogloboquadrina pachyderma* (%*N. pachyderma*; Fig. 3E; Becquey and Gersonde, 2003). This is in line with the suggestion of Huguet et al. (2013) that an increased OH-GDGT contribution results from an adaptation of the GDGT producing organisms, marine Archaea, to cold water.

3.2. Temperature reconstruction using existing GDGT calibrations

With the exception of two outliers, the recommended GDGT index for application in the subpolar region, TEX_{86}^{L}, yields temperature estimates in the range -1 to 17 °C when the Kim et al. (2010) global SST calibration is used ($SST_{TEX86\ L}$; Fig. 4A) or 0 to 14 °C when the Kim et al. (2012) TEX_{86}^{L} calibration with depth-integrated temperatures from 0 to 200 m water depth is applied ($SST_{TEX86\ L\ 0\text{-}200m}$; Fig. 4A). TEX_{86}^{L} temperatures are thus within the range of those inferred from alkenones and foraminiferal assemblages over most of the 500 kyr record but the temporal trends differ considerably from the other paleo-temperature proxies (Fig. 3A-C) and cold water mass indicators (Fig. 3D-F) from most intervals. TEX_{86}^{L} temperature corresponds well, however, to changes inferred from alkenones and foraminiferal assemblages during the last glacial cycle and MIS12–MIS10, but in contrast to other proxies does not exhibit any G-IG cycles during MIS 5 –10 (Fig. 4A).

The application of the Kim et al. (2010) global SST calibration for TEX_{86} (SST_{TEX86}), i.e. the original GDGT temperature index, yields temperature estimates in the range of 6 to 20 °C, consistently higher than from alkenones and foraminifera throughout the 500 kyr record (Fig.

232 4B). Average Holocene SST_{TEX86} values are also much higher than modern atlas SST and
233 Holocene average alkenones and foraminifera SST values (Table 2). Furthermore, G-IG
234 temporal trends in SST_{TEX86} are the opposite of other proxies at the site, with warmer glacial
235 than interglacial temperature (Fig. 4A). Neither TEX_{86}^{L} nor TEX_{86} correlated strongly with
236 SST_{UK37} in PS2489-2 (Fig. 5).

237 SST_{TEX86L} and SST_{TEX86} reconstructions may be biased by isoGDGTs of terrestrial origin for
238 samples with a branched and isoprenoid tetraether (BIT) index > 0.3 (Weijers et al., 2006), as
239 the BIT values along the core range between < 0.05 and 0.6. However, BIT swings between
240 high interglacial values and low glacial values (Fig. 3G), in an opposite trend from the
241 terrestrial indicators from dust (Fig. 2A) or ice rafted debris (IRD; Fig. 3F), and is driven
242 mainly by low crenarchaeol concentration during IG periods rather than the increase in
243 branched GDGT concentration during glacials (Fietz et al., 2011a). Bias due to inclusion of
244 samples with a BIT index > 0.3 is thus unlikely to explain the different temporal trends in the
245 TEX_{86} and TEX_{86}^{L} records vs. the other climate proxies.

246 Applying Huguet et al.'s (2013) global core top calibration for %OH (Eq. 2; $SST_{\%OH\ global}$)
247 gives temperature estimates that encompass the modern atlas SST (Fig. 4C), even though
248 Holocene $SST_{\%OH\ global}$ is, on average, 1.5 °C lower than modern atlas SST (Table 2).
249 Temporal trends in the $SST_{\%OH\ global}$ record (Fig. 4C) resemble those for $\%C_{37:4}$ (Fig. 4F).
250 Several important G-IG features observed in compilations of distinct archives around the
251 globe (e.g. Lang and Wolff, 2011) can be recognized in the $SST_{\%OH\ global}$ record, such as the
252 prominent increase in SST during Termination II at the onset of MIS 5 (Fig. 4C).
253 Furthermore, MIS 8 has been reported as a weak glacial stage in many records (e.g., Lang
254 and Wolff, 2011), and is apparent in our $SST_{\%OH\ global}$ record, even though, just as in other
255 marine and ice records, very low glacial temperature estimates are found at the onset of MIS
256 8 (Fig. 4C). MIS 2, particularly strong in the Jouzel et al. (2007) Dome C deuterium record

(Fig. 3C), is not notably colder according to the alkenones, foraminifera and OH-GDGT temperatures in PS2489-2 (Fig. 4C). Even the typical three sub-stage peaks occurring during interglacial MIS 7 (e.g. Lang and Wolff, 2011), not that obvious in SST_{UK37}, are represented in the $SST_{\%OH\ global}$ record, albeit by a limited number of data points (Fig. 4C). Within the three sub-peaks, sub-stage 7e has the highest $SST_{\%OH\ global}$, while sub-stages 7c and 7a are less pronounced, similar to the trends in the Dome C deuterium record. Almost glacial conditions were found in other records between the MIS 7 sub-stages (e.g. Lang and Wolff, 2011), which may not have been experienced that strongly at PS2489-2. The $SST_{\%OH\ global}$ record also coincides with the sharp increases observed in the Dome C deuterium record for MIS 5 and 9, immediately after the glacial termination, and the gradual increase observed during Termination V at the onset of MIS 11 (Fig. 4C).

Despite this good correspondence between %OH and known G-IG features, the amplitude of G-IG change in $SST_{\%OH\ global}$ is much larger than that in alkenone and foraminifera assemblage records, owing to much colder $SST_{\%OH\ global}$ during glacials (Fig. 4C; Fig. S2). Using the Arctic calibration (Eq. 3; $SST_{\%OH\ Arctic}$) the range of reconstructed SSTs narrows (Fig. 4D), but values are more than 2 °C lower than SST_{UK37} at the site throughout the past 500 kyr (Fig. S2). Moreover, both, global and Arctic calibrations produce unrealistic SST estimates below -5 °C (Fig. 4C-D). These sub-zero OH-GDGT-temperatures suggest the unsuitability of these existing calibrations for application at our study site.

3.3. Empirically exploring alternative OH-GDGT based temperature indices and calibrations

The two existing OH-GDGT calibrations applied above are based on limited sets of surface samples, which may have compromised their applicability for paleotemperature

281 reconstruction from core PS2489-2. To address this issue, we extended the data set by
282 combining the data from the global core top calibration (Huguet et al., 2013) and new data
283 from the Southern Ocean (Fig. 1; Table S1). In this new core top data set, relative abundances
284 of all iso- and OH-GDGTs show strong correlation with atlas SST (Table 1B; Fig. S1B). The
285 resultant regression of %OH vs. atlas SST in the new data set ($SST\%_{OHnew}$, Eq. 4 in Table S2)
286 is similar to that for the previous global calibration (Eq. 2). Therefore, applying it to PS2489-
287 2 results in similar temporal trends (Fig. 4E) to $SST_{\%OH\ global}$ (Fig. 4C) and those for $\%C_{37:4}$
288 (Fig. 4F). Again, the new calibration produces unrealistic sub-zero estimates (Fig. 4E).

289 Combinations of iso- and OH-GDGTs were then regressed against atlas SST to find the
290 combination with the best correlation following the empirical approach of Kim et al. (2010).
291 Different GDGT pools (Section 2.3) result in different best GDGT-temperature indices
292 (Table S3). Despite the strong correlation of Pool 1 and Pool 2 indices with overlying SST in
293 surface sediments (r^2 0.87 and 0.92, respectively; Table 3 and Eqs. 5 and 6 in Table S2), they
294 do not show the G-IG trends observed for alkenones and foraminifera from PS2489-2 (Figs.
295 6A-C) and, like TEX_{86}, Pool 1 does not correlate with SST_{UK37} from PS2489-2 (Fig. 5).
296 Furthermore, we note that the correlation of Pool 1 and Pool 2 indices with temperature is not
297 significantly greater than subsequently ranked indices (with r^2 values difference < 0.001;
298 Table S3), so a statistical justification for the preference of these indices is lacking.

299 As the above empirical approach fails to produce indices (that determine the reconstructed
300 temporal trends) and calibrations (that determine the reconstructed temperature values) which
301 result in expected G-IG changes in the sediment record, we explored here two indices based
302 on the a priori observation that the OH-GDGT relative abundances are related to low
303 temperature, as derived from the correlations with $\%C_{37:4}$, %*N. pachyderma*, Antarctic Dome
304 C temperature changes and SST_{UK37}. The first index (OH^L) uses the %OH index with a log
305 function similar to TEX_{86}^L (Eq. 7 in Table S2). The second index (OH^C) corresponds to an

extended TEX_{86} index modified similarly to the U^{K}_{37} index (Brassell et al., 1986), by subtracting the assumed cold water end member OH-GDGT-0 from the numerator (Eq. 8 in Table S2).

The OH^{C} index shows similarly good correlation with atlas SST as Pool 1 and Pool 2 in the core top data set, while the OH^{L} index shows a slightly weaker but significant correlation (Table 3). Temporal trends downcore for both indices, OH^{L} and OH^{C} (Fig. 6C-D), largely agree with those from other proxies for temperature and cold water presence (Fig. 3). The best correlation between GDGT derived temperature and alkenone derived temperature comes from the OH^{C} index (Fig. 5). It is probable that, as the relative contribution of these "cold water" compounds (OH-GDGTs) to the total GDGT pool increases as the temperature gets colder (Table 1; Fig. S1B), their inclusion in the indices allows a better quantification of the temperature effect. Interestingly, a better agreement with other proxies in down core trends obtained by applying U^{K}_{37} (alkenone unsaturation index, which includes cold water end member) instead of the more widely used $U^{K'}_{37}$ was reported for subpolar regions, namely the North Atlantic (Bard, 2001) and the Southern Ocean (Martínez-García et al., 2009; Ho et al., 2012). It is therefore not surprising that OH^{C}, constituted in a similar way, gives more realistic down core temporal trends than other empirical GDGT indices. However, again, the down core range of SST_{OHC} is greater than the ranges for other temperature proxies and strongly underestimates SST_{UK37} and $SSST_{foram}$ throughout most of the 500 kyr record, especially during glacial and transition periods (Fig. 6; Fig. S2).

Since the regression (slope and intercept) may change with the target temperature used for the calibration, next we examined if a different target temperature would result in more reasonable down core reconstruction. Regressing both new core top OH-GDGT indices to austral summer (January - March) SST did not change the regression intercept significantly (Fig. S3), so even the OH-GDGT-inferred summer SST values at PS2489-2 remain lower

than SST_{UK37} and $SSST_{foram}$ values (Fig. 6C-D). Adopting the subsurface provenance assumption suggested by Kim et al. (2012), we further re-calibrated our new core top data set to seawater temperature values integrated over the upper 0-200m (Fig. S3), which resulted in similar G-IG temperature variation as that inferred from the SST calibration (Fig. 6C-D). As the SST and 0-200 m calibrations are similar for temperature values < 10 °C (Fig. S3), the effect of such a re-calibration is therefore minor for the temperature range from core PS2489-2. In the following section, we discuss possible causative factors for sub-zero glacial temperature and large amplitude of the G-IG temperature change as inferred from OH-GDGT calibrations.

3.4. Why are OH-GDGT temperature values much colder than temperatures derived from alkenones and foraminifera during glacials?

In summary, at site PS2489-2, TEX_{86}, TEX_{86}^{L} and Pool 1 indices do not yield G-IG trends consistent with other proxies. In contrast, Pool 2, %OH, OH^{C} and OH^{L} indices show G-IG oscillations consistent with other proxies, but the values are unrealistic, especially during glacial stages where the estimated temperature values are too cold. Calibrating the index values to seasonal or subsurface water temperature does not improve the reconstructed temperature values. Our calibration might simply be unsuitable for quantifying G-IG water temperature at the site, plausibly caused by a limited range of index values. The subzero glacial OH-GDGT derived temperatures correspond to OH-GDGT index values that are beyond the index values observed in the modern core tops, so are in fact based on an extrapolation of the core top calibrations.

The resemblance between BIT index (Fig. 3G) and the $SST\%_{OH\ global}$ record (Fig. 4C) might indicate a (partly) terrestrial origin for the OH-GDGTs, which could bias the seawater

355 temperature reconstruction. However, the BIT and OH% indices (Fig. 2F) are negatively
356 correlated (R = -0.6, n = 116); the contribution of the OH-GDGTs is highest during the cold
357 glacial periods, when the BIT index is lowest. As mentioned above, the latter is mainly due to
358 low interglacial crenarchaeol concentration rather than high interglacial terrestrial input. In
359 contrast, the OH%-index does vary similarly in time with the dust and IRD input; the
360 contribution of the OH-GDGTs is highest during the cold glacial periods, when the IRD and
361 dust inputs are the highest. This indeed might suggest an eolian or ice edge related
362 provenance. Huguet et al (2013) found OH-GDGTs in both marine and fresh water settings.
363 A study in the Yellow Sea showed, however, that a large input of terrigenous organic matter
364 to the Yangtze Estuary had no significant influence on the OH-GDGT based proxy (Lü et al.,
365 2015). As Lü et al (2015) point out, OH-GDGTs have only been found in the marine
366 thaumarchaeal group I.1a (Pitcher et al. 2011; Liu et al., 2012a; Elling et al., 2014, 2015), but
367 not in terrestrial thaumarchaeal group I.1b (Sinninghe Damsté, 2012). Hence, a terrestrial
368 origin of the OH-GDGTs yet remains to be demonstrated. Consequently, the apparent
369 resemblance between the BIT and the $SST\%_{OH\ global}$ may be due to unrelated G-IG
370 environmental changes instead of a causal link between these parameters. We recommend
371 that the sources of the OH-GDGTs be further evaluated in future studies.

372 Another plausible explanation could be due to a difference in the recording season between
373 alkenone producing Haptophyceae, foraminifera and GDGT producing Archaea. The core top
374 U^{K}_{37} record at our site (Martínez-García et al., 2009) corresponds to warm season SST
375 values, likely because alkenones are produced primarily during warm seasons when their
376 production is not limited by light. Foraminiferal assemblages derived SST is calibrated to
377 summer SST. In contrast, winter peak abundances of pelagic Thaumarchaeota and/or GDGTs
378 have been observed in polar (Alonso-Saez et al., 2012) and other oceanic regions (e.g.
379 Wuchter et al., 2005; Galand et al., 2010; Bale et al., 2013). However, at site PS2489-2, the

modern temperature difference between coldest (September) and warmest (March) months is only ca. 2.3 °C (Locarnini et al., 2010), so a winter signal would be likely, but cannot by itself explain the offset > 5 °C, especially during glacials, between OH-GDGT temperature estimates and SST_{UK37} or $SSST_{foram}$.

A fourth plausible explanation refers to differences in depth habitat. While Wuchter et al. (2005) observed in a number of globally distributed oceanic regions that sedimentary GDGTs mainly originate from surface waters or the upper 100 m of the water column, other studies suggested that sedimentary GDGTs reflect subsurface temperature elsewhere (e.g. Huguet et al., 2007; Lopes dos Santos et al., 2010; Lengger et al., 2014). Kim et al. (2012) argued that, in the Southern Ocean, the GDGTs originate from the subsurface (0-200 m) rather than from the surface as Thaumarchaeota abundance often peaks at greater depth (e.g. 100-150 m; Karner et al., 2001). The comparison between average OH-GDGTs Holocene temperature estimates and the modern temperature profile at site PS2489-2 suggests an OH-GDGT provenance of > 100 m to as deep as 800 m. We note, however, the comparison of GDGT-inferred Holocene temperature to subsurface water temperature is only valid if we assume that the Holocene water column temperature profile was directly comparable with that in WOA09, and that the GDGT-temperature relationship at the sea surface is also true for the GDGTs produced in the mesopelagic water. The latter assumption may not always hold, because marine Archaea that thrive at depth may be genetically different from their counterpart in shallow water (e.g. Biller et al., 2012; Villanueva et al., 2014), and their GDGT distribution may differ, thereby resulting in a different GDGT-temperature relationship. Hence, GDGTs that occur at depth do not necessarily yield temperature values lower than those produced in shallower waters, as found in water column studies from various oceanographic settings (e.g. Schouten et al., 2012; Basse et al., 2014; Xie et al., 2014; Kim et al., 2015).

We cannot, however, eliminate the possibility of a shift in the recording and export depth between glacials and interglacials, as the cause of subzero temperature estimates and a large amplitude of G-IG temperature oscillation. Marine Archaea may shift their habitat during glacials to greater depth, for instance seeking refuge at greater depth against increasing competition with growing phytoplankton or due to a deepening of export depth. From TEX_{86} values of suspended particulate matter in the Santa Barbara Basin, Huguet et al. (2007) speculated that marine Archaea thrive at different water depths throughout the year, implying a temporally varying habitat depth for the marine Archaea. Assuming that such a habitat shift also occurs on longer time-scale, we postulate that marine Archaea may also live at different water depths through G-IG cycles. A deeper export depth of GDGTs during the Last Glacial Maximum in the eastern tropical Pacific was recently proposed by Hertzberg et al. (2016), based on the comparison of TEX_{86}^{H} temperatures with Mg/Ca-derived estimates measured on sea surface foraminifera and thermocline-dwelling foraminifera.

Finally, the relative contribution of shallow and deep water GDGTs to the sedimentary GDGT pool may also vary over G-IG cycles and this might explain why the glacial OH-GDGT values are beyond their modern global range in surface sediments. Under these circumstances, two different calibrations for interglacials and glacials, in accord with the marine archaeal habitat or export depth, would be needed in order to obtain realistic G-IG temperature variations. This requires, however, a much better understanding of the ecology of the OH-GDGT producing organisms and the GDGT export mechanisms in time and space.

4. Conclusions

TEX_{86} does not reproduce glacial-interglacial temperature changes recorded by other proxies at site PS2489-2 in the Subantarctic Atlantic over the last 500kyr. In contrast, TEX_{86}^{L}

temperature estimates are within the range of those inferred from alkenones and foraminifera proxies, although their G-IG temporal trends differ. However, the temporal variability in the percentage of OH-GDGTs is in good agreement with that of cold water mass indicators, $\%C_{37:4}$ and %*N. pachyderma*, as well as partially with dust deposition and IRD input. We therefore include the OH-GDGT in the temperature index and empirically derived and tested several indices based on an extended global core top data set. The OH-GDGT derived SST estimates are in good agreement with the temporal variability in foraminifera and alkenone SST throughout the 500 kyr record at PS2489-2. The best match of a OH-GDGT derived proxy with estimates from other approaches was observed for the new OH^C and OH^L index, where OH^C is a modified TEX_{86} index, by subtracting the assumed cold water end member OH-GDGT-0 from the numerator and OH^L includes a log function similar to $TEX_{86}{}^L$. The OH^C and OH^L indices may therefore potentially be used as a temperature proxy in the Southern Ocean, providing an alternative or complement to established proxies. Nevertheless, since the reconstructed OH-GDGT glacial temperature values are unrealistic, these indices should be further scrutinized and improved through laboratory culture experiments, a larger calibration data set and more down core applications, as well as a better understanding of OH-GDGT provenance and sedimentation.

Acknowledgments

S.F. and C.H. thank the Spanish Ministerio de Ciencia e Innovación (MICINN) for Juan de la Cierva fellowships. A SCAR Fellowship 2010/2011 is acknowledged for financially supporting the scientific stay of S.L.H. at the Universitat Autonoma de Barcelona. S.F. acknowledges support from South African National Research Foundation (grant number SNA14072378763). A.R.M. acknowledges support from the Spanish Research Ministry (CTM2013-43006). The authors thank R. Roux, Stellenbosch University, for re-analyses of some of the sample sets. We thank the editors S. Wakeham and J.R. Maxwell and two anonymous reviewers for their constructive comments.

Note: Core top and down core data will be archived on Pangaea, Data Publisher for Earth & Environmental Science (http://www.pangaea.de/) upon acceptance of the manuscript.

References

Alonso-Sáez, L., Waller, A.S., Mende, D.R., Bakker, K., Farnelid, H., Yager, P.L., Lovejoy, C., Tremblay, J-É., Potvin, M., Heinrich, F., Estrada, M., Riemann, L., Bork, P., Pedrós-Alió, C., Bertilsson, S., 2012. Role for urea in nitrification by polar marine Archaea. Proceedings of the National Academy of Sciences of the USA 109, 17989–17994.

Bale, N.J., Villanueva, L., Hopmans, E.C., Schouten, S., Sinninghe Damsté, J.S., 2013. Different seasonality of pelagic and benthic Thaumarchaeota in the North Sea. Biogeosciences 10, 7195-7206.

Bard, E., 2001. Comparison of alkenone estimates with other paleotemperature proxies. Geochemistry Geophysics Geosystems 2, 2000GC000050.

Basse, A., Zhu, C., Versteegh, G.J.M., Fischer, G., Hinrichs, K.-U., Mollenhauer, G., 2014. Distribution of intact and core tetraether lipids in water column profiles of suspended particulate matter off Cape Blanc, NW Africa. Organic Geochemistry 72, 1–13.

Becquey, S., Gersonde, R., 2002. Past hydrographic and climatic changes in the Subantarctic Zone of the South Atlantic - The Pleistocene record from ODP Site 1090. Palaeogeography, Palaeoclimatology. Palaeoecology 182, 221-239.

Becquey, S., Gersonde, R., 2003. A 0.55-Ma paleotemperature record from the Subantarctic Zone: Implications for Antarctic Circumpolar Current development. Paleoceanography 18, 1014.

Biller, S.J., Mosier, A.C., Wells, G.F., Francis, C.A., 2012. Global biodiversity of aquatic ammonia-oxidizing archaea is partitioned by habitat. Frontiers in Microbiology 3, 252.

Brassell, S.C., Eglinton, G., Marlowe, I.T., Pflaumann, U., Sarnthein, M., 1986. Molecular stratigraphy: a new tool for climatic assessment. Nature 320, 129-133.

480 Elling, F.J., Könneke, M., Lipp, J.S., Becker, K.W., Gagen, E.J., Hinrichs, K.-U., 2014.
481 Effects of growth phase on the membrane lipid composition of the thaumarchaeon
482 *Nitrosopumilus maritimus* and their implications for archaeal lipid distributions in the marine
483 environment. Geochimica et Cosmochimica Acta 141, 579–597.

484 Elling, F.J., Könneke, M., Mußmann, M., Greve, A., Hinrichs, K.-U., 2015. Influence of
485 temperature, pH, and salinity on membrane lipid composition and TEX_{86} of marine
486 planktonic thaumarchaeal isolates. Geochimica et Cosmochimica Acta 171, 238–255.

487 Etourneau, J., Collins, L.G., Willmott, V., Barbara, L., Leventer, A., Schouten, S., Sinninghe
488 Damsté, J.S., Bianchini, A., Klein, V., Crosta, X., Massé, G., 2013. Holocene climate
489 variations in the western Antarctic Peninsula: evidence for sea ice extent predominantly
490 controlled by changes in insolation and ENSO variability. Climate of the Past 9, 1431-1446.

491 Fietz, S., Martínez-Garcia, A., Huguet, C., Rueda, G., Rosell-Melé, A., 2011a. Constraints in
492 the application of the BIT index as a terrestrial input proxy. Journal of Geophysical Research
493 – Oceans 116, C10032.

494 Fietz, S., Martínez-Garcia, A., Rueda, G., Peck, V., Huguet, C., Escala, M., Rosell-Melé A.,
495 2011b. Crenarchaea and phytoplankton coupling in sedimentary archives: Common trigger or
496 metabolic dependence?. Limnology & Oceanography 56, 1907-1916.

497 Fietz, S., Huguet, C., Rueda, G., Hambach, B., Rosell-Melé, A., 2013. Hydroxylated
498 isoprenoidal GDGTs in the Nordic Seas. Marine Chemistry 152, 1-10.

499 Galand, P.E., Gutiérrez-Provecho, C., Massana, R., Gasol, J.M., Casamayor, E.O., 2010.
500 Inter-annual recurrence of archaeal assemblages in the coastal NW Mediterranean Sea
501 (Blanes Bay Microbial Observatory). Limnology & Oceanography 55, 2117–2125

Harris, P.G., Zhao, M., Rosell-Melé, A., Tiedemann, R., Sarnthein M., Maxwell, J.R., 1996. Chlorin accumulation rate as a proxy for Quaternary marine primary productivity. Nature 383, 63–65.

Hayes, C.T., Martínez-García, A., Hasenfratz, A., Jaccard, S.L., Hodell, D.A., Sigman, D.M., Haug G.H., Anderson R.F., 2014. A stagnation event in the deep South Atlantic during the last interglacial period. Science 346, 1514-1517.

Hertzberg, J.E., Schmidt, M.W., Smith, R.K., Shields, M.R., Bianchi, T.S., Marcantonio, F., 2016. Comparison of eastern tropical Pacific TEX_{86} and *Globigerinoides ruber* Mg/Ca derived sea surface temperatures: Insights from the Holocene and Last Glacial Maximum. Earth and Planetary Science Letters 434, 320-332.

Ho, S.L., Mollenhauer, G., Lamy, F., Martínez-García, A., Mohtadi, M., Gersonde, R., Hebbeln, D., Nunez-Ricardo, S., Rosell-Melé, A., Tiedemann, R., 2012. Sea surface temperature variability in the Pacific sector of the Southern Ocean over the past 700 kyr. Paleoceanography 27, PA4202.

Ho, S.L., Mollenhauer, G., Fietz, S., Martínez-García, A., Lamy, F., Rueda, G., Schipper, K., Méheust, M., Rosell-Melé, A., Stein, R., Tiedemann, R., 2014. Appraisal of TEX_{86} and TEX_{86}^{L} thermometries in subpolar and polar regions. Geochimica et Cosmochimica Acta 131, 213–226.

Hopmans E.C., Weijers, J.W.H., Schefuß, E., Herfort, L., Sinninghe Damsté, J.S., Schouten, S., 2004. A novel proxy for terrestrial organic matter in sediments based on branched and isoprenoid tetraether lipids. Earth Planetary Science Letters 22, 107–116.

Huguet, C., Schimmelmann, A., Thunell, R., Lourens, L.J., Sinninghe Damsté, J.S., Schouten, S., 2007. A study of the TEX_{86} paleothermometer in the water column and sediments of the Santa 538 Barbara Basin, California. Paleoceanography 22, PA3203.

526 Huguet, C., Fietz, S., Rosell-Melé, A., 2013. Global distribution patterns of hydroxy glycerol
527 dialkyl glycerol tetraethers. Organic Geochemistry 57, 107-118.

528 Jouzel, J., Masson-Delmotte, V., Cattani, O., Dreyfus, G., Falourd, S., Hoffmann, G., Minster
529 B., Nouet, J., Barnola, J.M., Chappellaz, J., Fischer, H., Gallet, J.C., Johnsen, S.,
530 Leuenberger, M., Loulergue, L., Luethi, D., Oerter, H., Parrenin, F., Raisbeck, G., Raynaud,
531 D., Schwander, J., Spahni, R., Souchez, R., Selmo, E., Schilt, A., Steffensen, J.P., Stenni, B.,
532 Stauffer, B., Stocker, T.F., Tison, J.L., Werner, M., Wolff, E.W., 2007. Orbital and millennial
533 Antarctic climate variability over the past 800,000 years. Science 317, 793-796.

534 Karner, M.B., DeLong, E.F., Karl, D.M., 2001. Archaeal dominance in the mesopelagic zone
535 of the Pacific Ocean. Nature 409, 507–510.

536 Kim, J.-H., Schouten, S., Hopmans, E.C., Donner, B., Sinninghe Damste, J.S., 2008. Global
537 sediment core-top calibration of the TEX_{86} paleothermometer in the ocean. Geochimica et
538 Cosmochimica Acta 72, 1154–1173.

539 Kim, J.H., van der Meer, J., Schouten, S., Helmke, P., Willmott, V., Sangiorgi, F., Koç, N.,
540 Hopmans, E.C., Sinninghe Damsté, J.S., 2010. New indices and calibrations derived from the
541 distribution of crenarchaeal isoprenoid tetraether lipids: implications for past sea surface
542 temperature reconstructions. Geochimica et Cosmochimica Acta 74, 4639–4654.

543 Kim, J.H., Crosta, X., Willmott, V., Renssen, H., Masse, G., Bonnin, J., Helmke, P.,
544 Schouten, S., Sinninghe Damsté, J.S., 2012. Increase in Late Holocene subsurface
545 temperature variability in East Antarctica. Geophysical Research Letters 39, L06705.

546 Kim, J.H., Schouten, S., Rodrigo-Gámiz, M., Rampen, S., Marino, G., Huguet, C., Helmke,
547 P., Buscail, R., Hopmans, E.C., Pross, J., Sangiorgi, F., Middelburg, J.B.M., Sinninghe
548 Damste J.S., 2015. Influence of deep-water derived isoprenoid tetraether lipids on the TEX_{86}

549 ^{H} paleothermometer in the Mediterranean Sea. Geochimica et Cosmochimica Acta 150, 125–
550 141.

551 Knies, J., Cabedo-Sanz, P., Belt, S.T., Baranwa, S., Fietz, S., Rosell-Melé, A., 2014. The
552 emergence of modern sea ice cover in the Arctic Ocean. Nature Communications 5, 5608.

553 Lambert, F., Delmonte, B., Petit, J.R., Bigler, M., Kaufmann, P.R., Hutterli, M.A., Stocker,
554 T.F., Ruth, U., Steffensen, J.P., Maggi, V., 2008. Dust-climate couplings over the past
555 800,000 years from the EPICA Dome C ice core. Nature 452, 616-619.

556 Lang, N., Wolff, E.W., 2011. Interglacial and glacial variability from the last 800 ka in
557 marine, ice and terrestrial archives. Climate of the Past 7, 361-380.

558 Lengger, S.K., Hopmans, E.C., Reichart, G.-J., Nierop, K.G.J., Sinninghe Damsté, J.S.,
559 Schouten, S., 2012. Intact polar and core glycerol dibiphytanyl glycerol tetraether lipids in
560 the Arabian Sea oxygen minimum zone. Part II: Selective preservation and degradation in
561 sediments and consequences for the TEX_{86}. Geochimica et Cosmochimica Acta 98, 244–258.

562 Lincoln, S.A., Wai, B., Eppley, J.M., Church, M.J., Summons, R.E., DeLong, E.F., 2014a.
563 Planktonic Euryarchaeota are a significant source of archaeal tetraether lipids in the ocean.
564 Proceedings of the National Academy of Sciences of the USA 111, 9858-63.

565 Lincoln, S.A., Wai, B., Eppley, J.M., Church, M.J., Summons, R.E., DeLong, E.F., 2014b.
566 Reply to Schouten et al.: Marine Group II planktonic Euryarchaeota are significant
567 contributors to tetraether lipids in the ocean. Proceedings of the National Academy of
568 Sciences of the USA 111, E4286.

569 Lisiecki, L.E., Raymo, M.E., 2005. A Pliocene-Pleistocene stack of 57 globally distributed
570 benthic δ18O records. Paleoceanography 20, PA1003.

571 Liu, X.-L., Lipp, J.S., Simpson, J.H., Lin, Y.-S., Summons, R.E., Hinrichs, K.-U., 2012a.
572 Mono and dihydroxyl glycerol dibiphytanyl glycerol tetraethers in marine sediments:
573 identification of both core and intact polar lipid forms. Geochimica et Cosmochimica Acta
574 89, 102–115.

575 Liu, X.-L., Summons, R.E., Hinrichs, K.-U., 2012b. Extending the known range of glycerol
576 ether lipids in the environment: structural assignments based on tandem mass spectral
577 fragmentation patterns. Rapid Communications in Mass Spectrometry 26, 2295–2302.

578 Locarnini, R.A., Mishonov, A.V., Antonov, J.I., Boyer, T.P., Garcia, H.E., Baranova, O.K.,
579 Zweng, M.M., Johnson, D.R., 2010. World Ocean Atlas 2009, Volume 1: Temperature. In:
580 Levitus, S. (Ed.), NOAA Atlas NESDIS 68, U.S. Government Printing Office, Washington,
581 D.C., 184 pp.

582 Lopes dos Santos, R.A., Prange, M., Castañeda, I.S., Schefuß, E., Mulitza, S., Schulz, M.,
583 Niedermeyer, E.M., Sinninghe Damsté, J.S., Schouten, S., 2010. Glacial-interglacial
584 variability in Atlantic meridional overturning circulation and thermocline adjustments in the
585 tropical North Atlantic. Earth and Planetary Science Letters 300, 407-414.

586 Lü, X., Liu, X.-L., Elling, F.J., Yang, H., Xie, S., Song, J., Li, X., Yuan, H., Li, N., Hinrichs,
587 K.-U., 2015. Hydroxylated isoprenoid GDGTs in Chinese coastal seas and their potential as a
588 paleotemperature proxy for mid-to-low latitude marginal seas. Organic Geochemistry 89-90,
589 31-43.

590 Martínez-García, A., Rosell-Melé, A., Geibert, W., Gersonde, R., Masqué, P., Gaspari, V.,
591 Barbante, C., 2009. Links between iron supply, marine productivity, sea surface temperatures
592 and CO2 over the last 1.1My. Paleoceanography 24, PA1207.

593 Martínez-García, A., Rosell-Mele, A., McClymont, E.L., Gersonde, R., Haug, G.H., 2010.
594 Subpolar link to the emergence of the Modern Equatorial Pacific cold tongue. Science 328,
595 1550 – 1553.

596 Martínez-García, A, Sigman, D.M., Ren, H., Anderson, R.F., Straub, M., Hodell, D.A.,
597 Jaccard, S.L., Eglinton, T.I., Haug, G.H., 2014. Iron fertilization of the Subantarctic Ocean
598 during the last ice age. Science 343, 1347-1350.

599 Pitcher, A., Hopmans, E.C., Mosier, A.C., Park, S.-J., Rhee, S.-K., Francis, C.A., Schouten,
600 S., Sinninghe Damsté, J.S., 2011. Core and intact polar glycerol dibiphytanyl glycerol
601 tetraether lipids of ammonia-oxidizing archaea enriched from marine and estuarine
602 sediments. Applied and Environmental Microbiology 77, 3468–3477.

603 Rosell-Melé, A., 1998. Interhemispheric appraisal of the value of alkenone indices as
604 temperature and salinity proxies in high-latitude locations. Paleoceanography 13, 694-703.

605 Schlitzer, R., 2014. Ocean Data View. <http://www.awi-bremerhaven.de/GEO/ODV>.

606 Schouten, S., Hopmans, E.C., Schefuss, E., Sinninghe Damsté, J.S., 2002. Distributional
607 variations in marine crenarchaeotal membrane lipids: a new tool for reconstructing ancient
608 sea water temperatures?. Earth and Planetary Science Letters 204, 265–274.

609 Schouten, S., Hopmans, E.C., Sinninghe Damsté, J.S., 2013. The organic geochemistry of
610 glycerol dialkyrl glycerol tetraether lipids: a review. Organic Geochemistry 54, 19–61.

611 Schouten S., Pitcher, A., Hopmans, E.C., Villanueva, L., van Bleijswijk, J., Sinninghe
612 Damsté, J.S., 2012. Intact polar and core glycerol dibiphytanyl glycerol tetraether lipids in the
613 Arabian Sea oxygen minimum zone: I. Selective preservation and degradation in the water
614 column and its consequences for the TEX_{86}. Geochimica et Cosmochimica Acta 98, 228-243.

615 Schouten, S., Villanueva, L., Hopmans, E.C., van der Meer, M.T.J., Sinninghe Damsté, J.S.,
616 2014. Are Marine Group II Euryarchaeota significant contributors to tetraether lipids in the
617 ocean? Proceedings of the National Academy of Sciences of the USA 111, E4285

618 Shevenell, A.E., Ingalls, A.E., Domack E.W., Kelly, C., 2011. Holocene Southern Ocean
619 surface temperature variability west of the Antarctic Peninsula. Nature 470, 250–254.

620 Sinninghe Damsté, J.S., Rijpatra, W.I.C., Hopmans, E.C., Jung, M.-Y., Kim, J.-G., Rhee, S.-
621 K., Stieglmeier, M., Schleper, C., 2012. Intact polar and core glycerol dibiphytanyl glycerol
622 tetraether lipids of Group 1.1a and 1.1b Thaumarchaeota in soil. Applied and Environmental
623 Microbiology 78, 6866– 6874.

624 Villanueva, L., Schouten, S., Sinninghe Damsté, J.S., 2014. Depth-related distribution of a
625 key gene of the tetraether lipid biosynthetic pathway in marine Thaumarchaeota.
626 Environmental Microbiology 17, 3527-3539.

627 Weijers, J.W.H., Schouten, S., Spaargaren, O.C., Sinninghe Damsté, J.S., 2006. Occurrence
628 and distribution of tetraether membrane lipids in soils: Implications for the use of the TEX_{86}
629 proxy and the BIT index. Organic Geochemistry 37, 1680-1693.

630 Wuchter, C, Schouten, S., Wakeham, S.G., Sinninghe Damsté, J.S., 2005. Temporal and
631 spatial variation in tetraether membrane lipids of marine Crenarchaeota in particulate organic
632 matter: implications for TEX_{86} paleothermometry. Paleoceanography 20, PA3013.

633 Xie, S., Liu, X.-L., Schubotz, F., Wakeham, S.G., Hinrichs, K.-U., 2014. Distribution of
634 glycerol ether lipids in the oxygen minimum zone of the Eastern Tropical North Pacific
635 Ocean. Organic Geochemistry 71, 60-71.

Tables

Table 1

Correlation between GDGT fractional abundances (out of total pool of isoprenoid GDGTs) vs. SST (°C); (A) Along PS2489-2 record; SST derived from alkenone unsaturation index (SST_{UK37}; Martínez-García et al., 2009) and (B) In core-top compilation; SST extracted from World Ocean Atlas 09 (SST_{WOA}; Locarnini et al., 2010)[a].

(A) vs SST_{UK37}	r	p
GDGT-0	0.330	< 0.001
GDGT-1	0.555	< 0.0001
GDGT-2	0.519	< 0.0001
GDGT-3	-0.039	> 0.1
GDGT-5	-0.307	< 0.001
GDGT-5'	0.021	> 0.1
OH-GDGT-0	-0.500	< 0.0001
OH-GDGT-1	-0.369	< 0.0001
OH-GDGT-2	-0.096	> 0.1

(B) vs SST_{WOA09}	r	p
GDGT-0	-0.894	< 0.0001
GDGT-1	0.588	< 0.0001
GDGT-2	0.891	< 0.0001
GDGT-3	0.714	< 0.0001
GDGT-5	0.884	< 0.0001
GDGT-5'	0.755	< 0.0001
OH-GDGT-0	-0.881	< 0.0001
OH-GDGT-1	-0.447	< 0.001
OH-GDGT-2	0.482	< 0.001

[a] Plots are shown in Supplementary Material Fig. S1A (vs. SST_{UK37}) and S1B (vs. SST_{WOA}). N= 52 for regressions vs. SST_{WOA} and n= 114 for regressions vs. SST_{UK37}.

644 **Table 2**

645 Reconstructed Holocene (< 10 ky) temperature (°C) derived from alkenones (data from
646 Martínez-García et al., 2009) and foraminifera (data from Becquey and Gersonde, 2003) as
647 well as from various GDGT-indices (see main text for details). Average Holocene
648 temperatures and standard deviations are given. Five samples have been included for
649 alkenone- and GDGT-indices and seven for foraminifera. For comparison: modern annual
650 mean atlas SST is 10.0 °C, modern winter avg. 9.2 °C and modern summer avg. 10.9 °C (0
651 m; WOA09; Locarnini et al., 2010).

652

	Holocene Temperature (°C)	
	Avg.	Standard deviation
U^{K}_{37}	13.37	1.45
Foraminifera	10.30	0.67
TEX_{86}	15.42	2.14
TEX_{86}^{L}	15.73	2.05
TEX_{86}^{L} (0-200m)	12.64	1.54
$OH\%_{global}$	8.52	5.65
$OH\%_{Arctic}$	3.50	2.02
$OH\%_{new}$	2.35	7.49
Pool 1	11.95	2.89
Pool 2	6.52	5.21
OH^{C}	6.15	3.86
OH^{C} (summer)	7.58	4.00
OH^{C} (0-200m)	4.84	3.08
OH^{L}	2.16	5.21
OH^{L} (summer)	3.23	5.32
OH^{L} (0-200m)	1.49	4.18

653

Table 3

Core top GDGT indices correlated with (A) atlas annual mean SST ($SST_{WOA\ 0m}$), as well as (B) summer SST ($SSST_{WOA\ 0m}$) and (C) subsurface temperature integrated over 0-200 m ($SST_{WOA\ 0\text{-}200m}$) at core top sites (see Fig. 1). All temperature data are from World Ocean Atlas 09 (Locarnini et al., 2010). Pools 1 and 2 indicate two different GDGT pools, i.e. Pool 1, All TEX_{86} GDGTs; Pool 2, All TEX_{86} GDGTs plus all OH-GDGTs. OH^C and OH^L indicate indices modified with a priori observation that relative abundance of OH-GDGTs is related to cold water. The OH^C-index is a modified TEX_{86} index by subtracting the assumed cold water end member OH-GDGT-0 from the numerator (Table S2). The OH^L-index is the %OH with a log function similar to TEX_{86}^L (Table S2). Regression plots and equations are shown in Fig. S3; rse, residual standard error.

(A) vs. $SST_{WOA\ 0m}$	r^2	rse	p
TEX_{86}	0.780	0.059	< 0.0001
TEX^{L}_{86}	0.858	0.048	< 0.0001
%OH	0.740	1.150	< 0.0001
Pool 1	0.873	0.257	< 0.0001
Pool 2	0.916	0.094	< 0.0001
OH^{C}	0.882	0.104	< 0.0001
OH^{L}	0.736	0.128	< 0.0001

(B) vs. $SSST_{WOA\ 0m}$	r^2	rse	p
TEX_{86}	0.738	0.065	< 0.0001
TEX^{L}_{86}	0.843	0.050	< 0.0001
%OH	0.777	1.066	< 0.0001
Pool 1	0.868	0.262	< 0.0001
Pool 2	0.912	0.096	< 0.0001
OH^{C}	0.882	0.104	< 0.0001
OH^{L}	0.761	0.121	< 0.0001

(C) vs. $SST_{WOA\ 0-200m}$	r^2	rse	p
TEX_{86}	0.745	0.064	< 0.0001
TEX^{L}_{86}	0.836	0.051	< 0.0001
%OH	0.713	1.208	< 0.0001
Pool 1	0.853	0.276	< 0.0001
Pool 2	0.881	0.112	< 0.0001
OH^{C}	0.846	0.119	< 0.0001
OH^{L}	0.689	0.138	< 0.0001

665

Figures

Fig. 1. (**A**) Locations of core tops used for calibration of GDGT proxies from tropical-temperate regions and Arctic Ocean (Huguet et al., 2013; crosses), Pacific Southern Ocean (Ho et al., 2014, and this study; open diamonds), as well as sediment core PS2489-2 in the subantarctic Southern Ocean (yellow star). Background colours indicate annual mean sea surface (0 m depth) temperature (°C). (**B**) Latitudinal depth section of temperature in the Atlantic Southern Ocean (averaged over the area of the dashed rectangle in Fig. 1A) illustrating the present temperature and location (yellow star) of core PS2489-2. Colours indicate temperature values (°C). (**C**) Temperature profiles for annual mean (black curve), winter (July – September; blue curve) and summer (January – March; green curve) at site PS2489-2. Also indicated are average reconstructed Holocene temperatures (see Table 2) for the temperature indices discussed in this study that fall into the range of the modern temperature (e.g., average estimated Holocene SST_{UK37} is 13.4 °C, which exceeds the modern temperature range at site PS2489-2). The maps were produced using the Ocean Data View software 4.6.3.1 (Schlitzer et al., 2014) and World Ocean Atlas 2009 data (WOA09; Locarnini et al., 2010).

Fig. 2. Glacial-interglacial variability in Atlantic subantarctic over the past ca. 500 ky. **(A**) Dust concentration in Antarctic EPICA Dome C (EDC) ice record (data from Lambert et al., 2008), (**B**) Concentrations of alkenones (indicating productivity of alkenone producers such as coccolithophores) in PS2489-2 record (Martínez-García et al, 2009), (**C**) Concentration of chlorins (indicating export productivity) in PS2489-2 record (Fietz et al., 2011b), (**D**) Concentrations of isoGDGTs (ranging from 2.41 – 1234 ng/g dry sediment), (**E**) Concentrations of OH-GDGTs (ranging from 0.538 – 116 ng/g dry sediment), (**F**) Relative abundance of OH-GDGTs to the sum of iso- and OH-GDGTs (%OH). Shaded rectangles indicate approximate glacial stages with numbers above shaded rectangles indicating

respective marine isotopic stages (MISs) following the definition of Lisiecki and Raymo (2005). Three-point running averages are shown (thick lines) for all records to facilitate the visualisation of the data.

Fig. 3. Glacial-interglacial variability in temperature proxies and cold water mass indicators for the subantarctic Atlantic over the past ca. 500 ky. (**A**) Sea surface temperature reconstruction based on U^{K}_{37} (SST_{UK37}; data from Martínez-García et al., 2009). (**B**) Summer sea surface temperature reconstruction derived from planktonic foraminiferal associations ($SSST_{foram}$; data from Becquey and Gersonde, 2003). (**C**) Change in temperature in Antarctic EPICA Dome C (EDC) ice record (data from Jouzel et al., 2007). (**D)** Relative abundance (%) of $C_{37:4}$ alkenones to total C_{37} alkenones in PS2489-2 record indicating cold water mass influence (data from Martínez-García et al., 2009). (**E**) Relative abundance of sinistral coiling *N. pachyderma*, a cold-water species, dwelling predominantly in water with < 6 to 8 °C (data from Becquey and Gersonde, 2002). The relative abundance is given in % per total of four foraminifera species that dominate the planktonic foraminiferal assemblage in PS2489-2 record. (**F**) Ice rafted debris (IRD) concentration in PS2489-2 record (data from Becquey and Gersonde, 2002) indicating presence of icebergs at site PS2489-2. (**G**) BIT index calculated as per Hopmans et al. (2004). Shaded rectangles indicate approximate glacial stages with numbers above shaded rectangles indicating respective marine isotopic stages (MISs) following the definition of Lisiecki and Raymo (2005). Thin lines represent data points, while three-point running averages are shown (thick lines) for all records to facilitate the visualisation of the data..

Fig. 4. Water temperature reconstruction over five glacial-interglacial cycles at PS2489-2. (**A**) Based on TEX_{86}^{L} using core top calibration for surface waters from Kim et al. (2010; SST_{TEX86L}; orange lines) and subsurface waters from Kim et al. (2012; $subSST_{TEX86L\ 0\text{-}200m}$; green lines) and (**B**) Based on TEX_{86} using core top calibrations from Kim et al. (2010;

716 SST_{TEX86}; brown lines). (**C)** Based on %OH index and Huguet et al. (2013) global calibration
717 ($SST_{\%OH\ global}$; red lines) or (**D**) on %OH index and Fietz et al. (2013) Arctic core top
718 calibration ($SST_{\%OH\ Arctic}$; blue lines) or (**E**) on %OH index and new calibration presented
719 here (green lines). (**F**) Relative abundance (%) of $C_{37:4}$ alkenones to total C_{37} alkenones in
720 PS2489-2 record indicating cold water mass influences for reference (data from Martínez-
721 García et al., 2009; purple lines). Thin lines represent data points, while three-point running
722 averages are shown (thick lines) for all records to facilitate the visualisation of the data. .
723 Panels 4A to 4E show SST_{UK37} (dark gray lines) and $SSST_{foram}$ (light gray lines) in the
724 background at the same scale as respective GDGT-SST. Shaded rectangles indicate
725 approximate glacial stages with numbers above shaded rectangles indicating respective
726 marine isotopic stages (MISs) following the definition of Lisiecki and Raymo (2005). Dashed
727 horizontal lines in panel A to E indicate modern annual mean atlas SST (ca. 10 °C; derived
728 from World Ocean Atlas 2009 data (Locarnini et al., 2010)).

729 **Fig. 5.** Correlations between GDGT- indices and SST_{UK37} from core PS2489-2.

730 **Fig. 6.** Water temperature reconstruction over five glacial-interglacial cycles at PS2489-2
731 based on: **(A**) Pool 1-index (best core top index including only TEX_{86} GDGTs, Table S3;
732 green lines), (**B**) Pool 2-index (best core top index including TEX_{86}- and OH-GDGTs, Table
733 S3; brown lines). (**C**) OH^L index derived annual mean (orange lines) and summer (yellow
734 lines) for surface waters or subsurface waters (green lines); OH^L index is similar to $TEX_{86}{}^L$
735 index but includes the OH-GDGTs (Table S2). **(D**) OH^C index derived annual mean (blue
736 lines) and summer (light blue lines) for surface waters or subsurface waters (dark blue lines) ;
737 OH^C index is similar to TEX_{86} index modified similarly to the U^K_{37}, by subtracting assumed
738 cold-water end member OH-GDGT-1 from the numerator (Table S2). Three Thin lines
739 represent data points, while three-point running averages are shown (thick lines) for all
740 records to facilitate the visualisation of the data. . All panels show SST_{UK37} (dark gray lines)

741 and $SSST_{foram}$ (light gray lines) in the background at the same scale as respective GDGT-SST
742 or -subSST. Shaded background rectangles indicate glacial stages with numbers above
743 shaded rectangles indicating respective marine isotopic stages (MISs) following the definition
744 of Lisiecki and Raymo (2005).

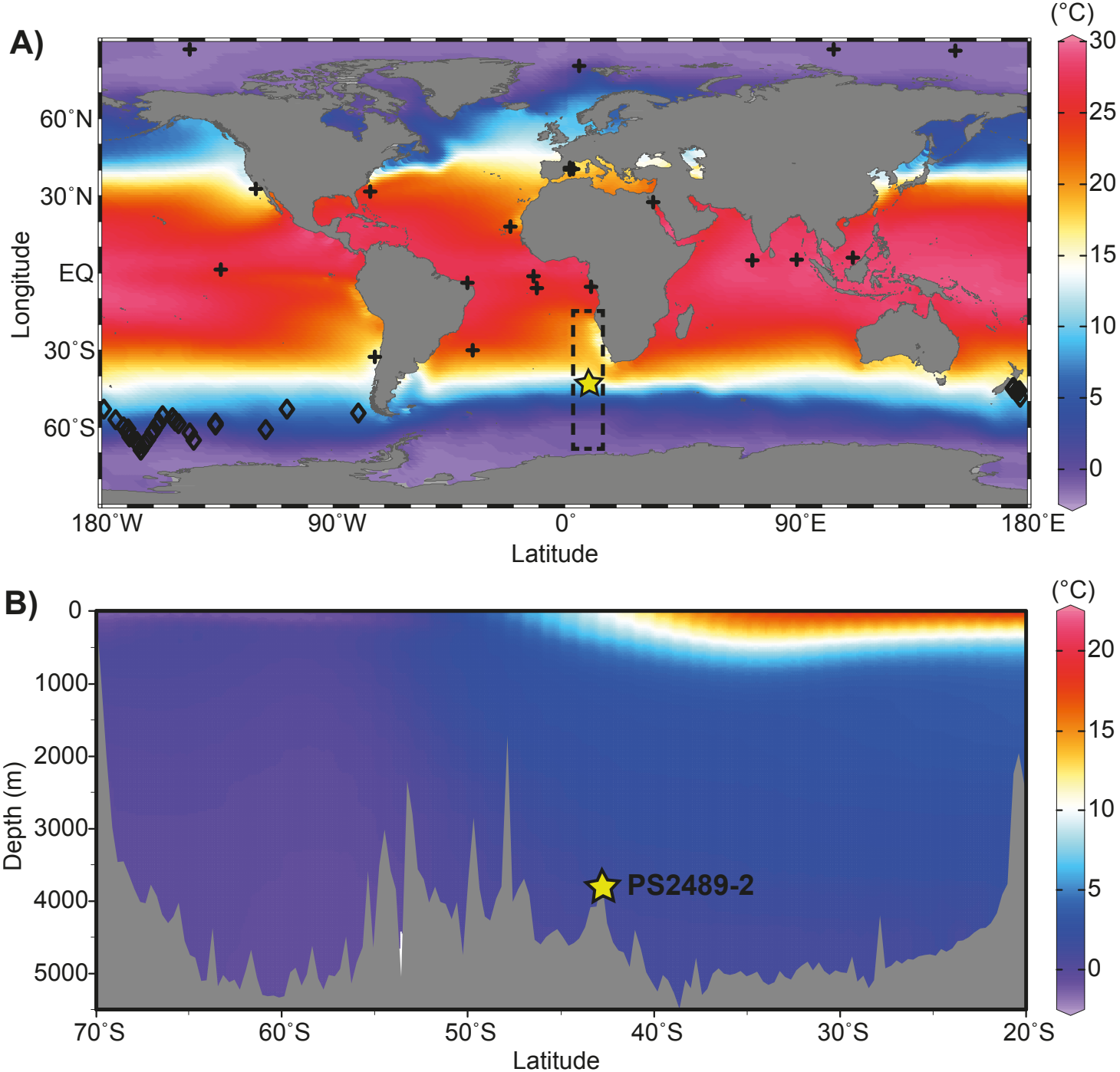
A)
(°C)
30
25
20
15
10
5
0
60˚N
30˚N
EQ
30˚S
60˚S
Longitude
180˚W
90˚W
0˚
90˚E
180˚E
Latitude
B)
(°C)
20
15
10
5
0
0
1000
2000
3000
4000
5000
Depth (m)
PS2489-2
70˚S
60˚S
50˚S
40˚S
30˚S
20˚S
Latitude
C)
Modern annual mean
Modern summer
Modern winter
Holocene SST foraminifera
Holocene SST Pool1
Holocene SST %OG global
Holocene SST OH C(Summer)
Holocene SST Pool2
Holocene SST OH C
Holocene subSST OH C(0–200m)
Holocene SST %OH Arctic
0
200
400
600
800
1000
Depth (m)
2
4
6
8
10
12
Seawater temperature (°C)

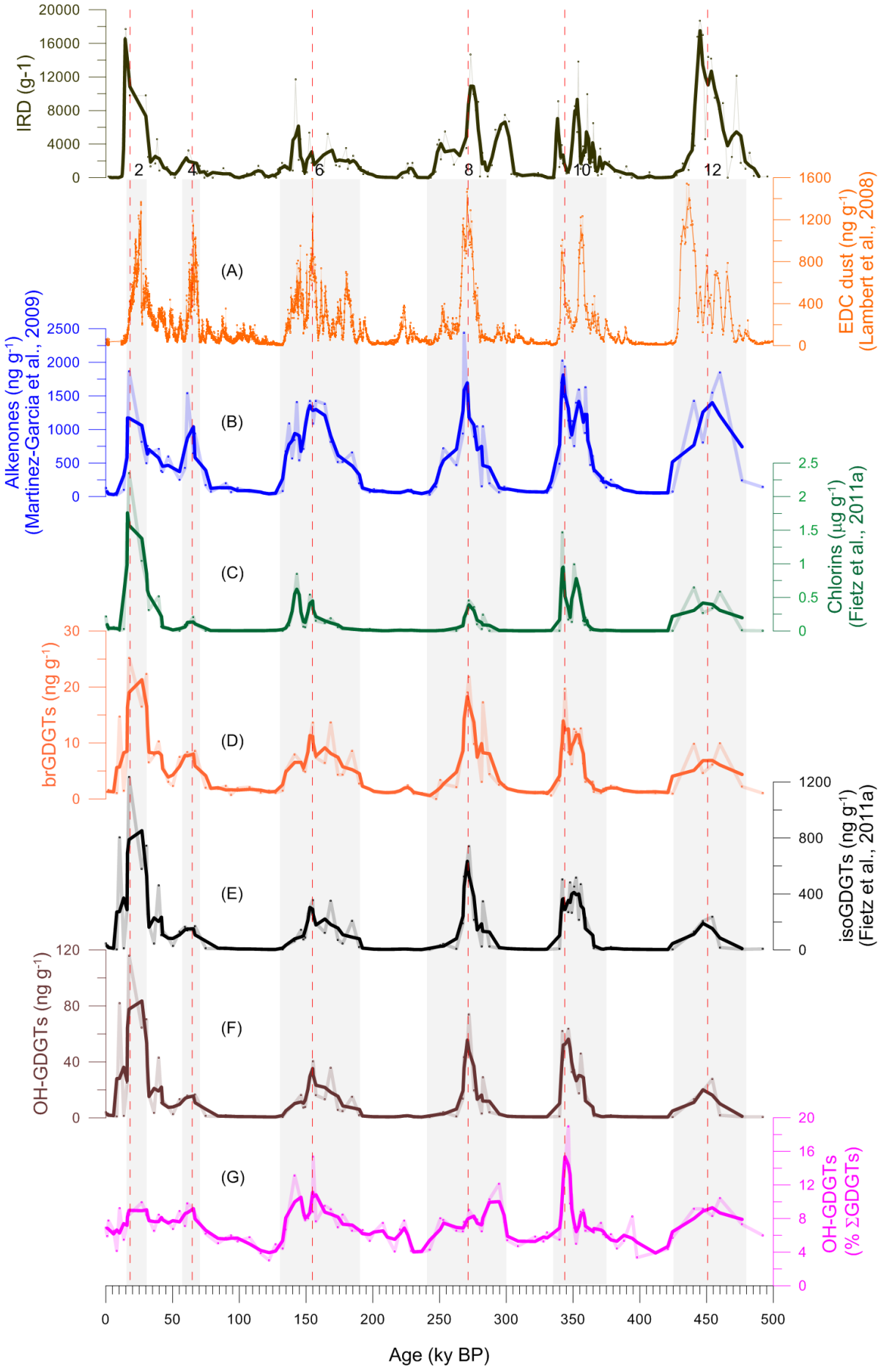
IRD (g-1)
20000
16000
12000
8000
4000
0
2
4
6
8
10
12
(A)
EDC dust (ng g-1)
(Lambert et al., 2008)
1600
1200
800
400
0
Alkenones (ng g-1)
(Martinez-Garcia et al., 2009)
2500
2000
1500
1000
500
0
(B)
(C)
Chlorins (µg g-1)
(Fietz et al., 2011a)
2.5
2
1.5
1
0.5
0
brGDGTs (ng g-1)
30
20
10
0
(D)
(E)
isoGDGTs (ng g-1)
(Fietz et al., 2011a)
1200
800
400
0
OH-GDGTs (ng g-1)
120
80
40
0
(F)
(G)
OH-GDGTs
(% ΣGDGTs)
20
16
12
8
4
0
0
50
100
150
200
250
300
350
400
450
500
Age (ky BP)

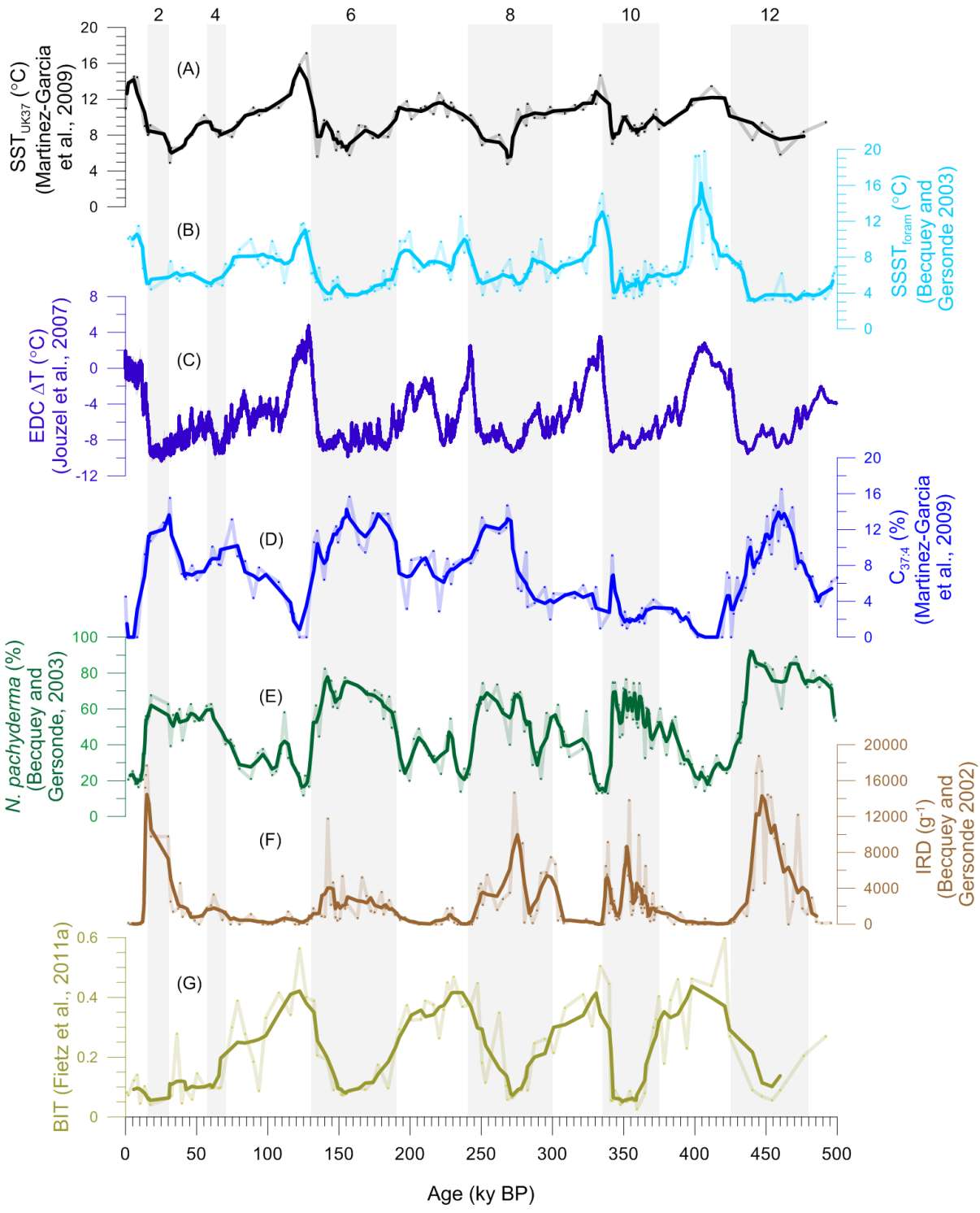
2
4
6
8
10
12
(A)
SST$_{UK37}$ (°C)
(Martinez-Garcia et al., 2009)
(B)
SSST$_{foram}$ (°C)
(Becquey and Gersonde 2003)
(C)
EDC ΔT (°C)
(Jouzel et al., 2007)
(D)
$C_{37:4}$ (%)
(Martinez-Garcia et al., 2009)
(E)
N. pachyderma (%)
(Becquey and Gersonde, 2003)
(F)
IRD (g^{-1})
(Becquey and Gersonde 2002)
(G)
BIT (Fietz et al., 2011a)
Age (ky BP)

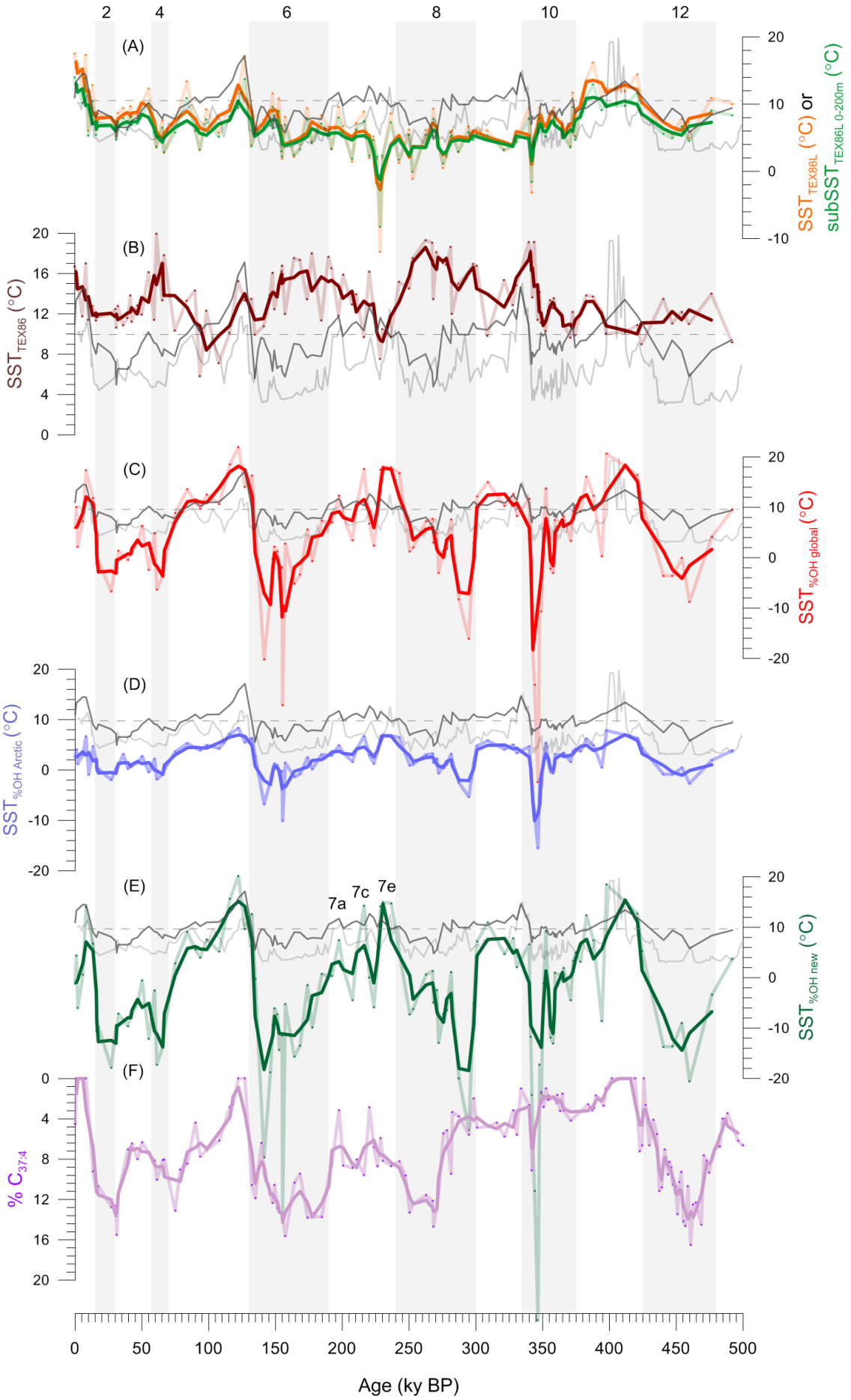
2
4
6
8
10
12
(A)
(B)
(C)
(D)
(E)
(F)
7a
7c
7e
SST$_{TEX86L}$ (°C) or subSST$_{TEX86L\ 0\text{-}200m}$ (°C)
SST$_{TEX86}$ (°C)
SST$_{\%OH\ global}$ (°C)
SST$_{\%OH\ Arctic}$ (°C)
SST$_{\%OH\ new}$ (°C)
% C$_{37:4}$
Age (ky BP)

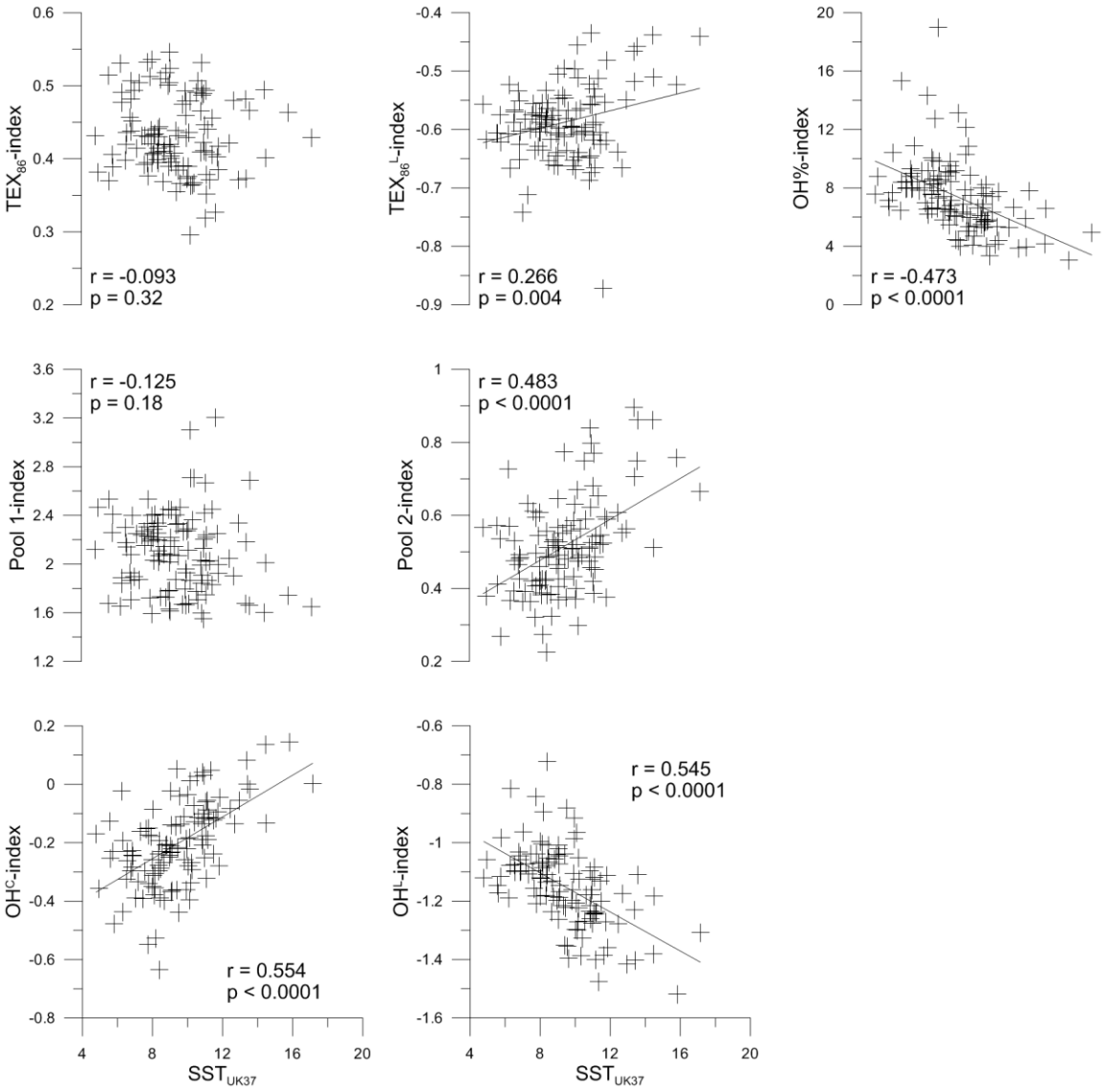
TEX86-index
r = -0.093
p = 0.32
TEX86L-index
r = 0.266
p = 0.004
OH%-index
r = -0.473
p < 0.0001
Pool 1-index
r = -0.125
p = 0.18
Pool 2-index
r = 0.483
p < 0.0001
OHC-index
r = 0.554
p < 0.0001
OHL-index
r = 0.545
p < 0.0001
SSTUK37
SSTUK37

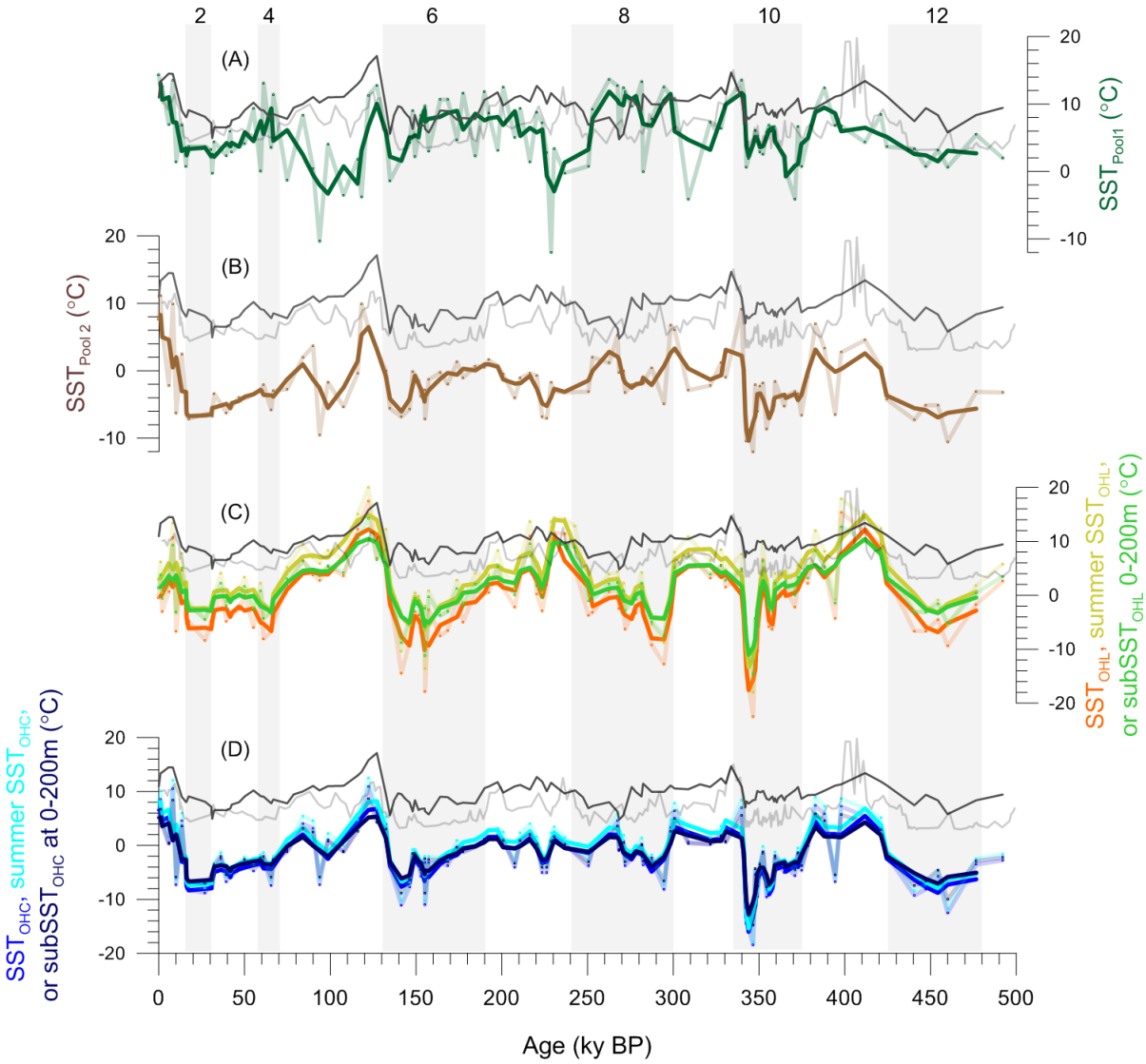
2
4
6
8
10
12
(A)
(B)
(C)
(D)
20
10
0
-10
-20
SST$_{Pool1}$ (°C)
SST$_{Pool 2}$ (°C)
SST$_{OHL}$, summer SST$_{OHL}$, or subSST$_{OHL}$ 0-200m (°C)
SST$_{OHC}$, summer SST$_{OHC}$, or subSST$_{OHC}$ at 0-200m (°C)
0
50
100
150
200
250
300
350
400
450
500
Age (ky BP)

Supplementary Material

for

Appraising GDGT-based seawater temperature indices in the Southern Ocean

Organic Geochemistry, 2016, http://dx.doi.org/10.1016/j.orggeochem.2016.10.003

S. Fietz[a†*], S.L. Ho[b†,1], C. Huguet[c], A. Rosell-Melé[c,d], A. Martínez-García[e]

[a]*Department of Earth Sciences, Stellenbosch University, Stellenbosch, South Africa*

[b]*Alfred Wegener Institute, Helmholtz Centre for Polar and Marine Research, Potsdam, Germany*

[c]*Institut de Ciència i Tecnologia Ambientals, Universitat Autònoma de Barcelona, Bellaterra, Catalonia, Spain*

[d]*Institució Catalana de Recerca i Estudis Avançats, Barcelona, Catalonia, Spain*

[e]*Geological Institute, Swiss Federal Institute of Technology Zürich, Zürich, Switzerland*

[†]These authors contributed equally to the study.

*Corresponding author: *E-mail* address s_fietz@web.de (S. Fietz).

[1.]Present address: Bjerknes Centre for Climate Research and University of Bergen, Allegaten 41, 5007 Bergen, Norway.

Contents of this file

Figures S1 to S3
Tables S1 to S3

Introduction

Our compilation contains 52 surface sediment samples. The Support Information contains the core-top data in Table S1 including where data were published previously. The samples were taken from three sample batches: (i) tropical-temperate from our archives (details given by Huguet et al., 2013), (ii) Arctic Ocean collected during R/V Polarstern expedition ARK-XXIII/1 (Huguet et al., 2013), and (iii) Pacific Southern Ocean collected during R/V Polarstern voyage ANT-XXVI/2 (as described by Ho et al., 2014). These core-top data and the data for sediment core PS2489-2 will be made available through Pangaea, Data Publisher for Earth & Environmental Science, www.pangaea.de. Site location for surface sediments and PS2489-2 are shown in the main article Figure 1.

Table S2 shows all alternative OH-GDGT-based indices tested in this study including their calibrations against WOA09-SST. These calibrations are used in the plots shown in Figure 6 of the main manuscript.

Table S3 shows the top five combinations which have the strongest correlation with WOA09-SST for two pools of GDGTs (where Pool 1 consists of only TEX_{86} GDGTs and Pool 2 of TEX_{86} GDGTs and OH-GDGTs; Sections 2.3 and 3.3 of the main manuscript).

Figures S1A and S1B show the correlations between the relative abundances of each GDGT with modern SST or with paleotemperature derived from alkenones. Each GDGT is labelled according to their number of rings, e.g. GDGT-0 is the acyclic GDGT with *m/z* 1302. This naming convention follows previous GDGT calibration studies, such as Kim et al. (2010) and Ho et al. (2014). GDGT-5 is crenarchaeol and GDGT-5' the crenarchaeol regioisomer. Structures for the isoprenoid GDGTs are given, for instance, by Kim et al. (2010). Labelling of OH-GDGTs follows similar logic with OH-GDGT-0 being acyclic while OH-GDGT-1 has 1 ring etc. Structures for OH-GDGTs are given by Liu et al. (2012) and Huguet et al. (2013).

Figure S2 visualizes the difference between the modelled temperature based on OH-GDGT indices and SST_{UK37} (ΔSST (°C) = $SST_{OH\%}$ - SST_{UK37}) indicating the SST underestimation using the GDGT-paleothermometry compared to the alkenone-paleothermometry.

Figure S3 shows the correlation between the core-top GDGT indices and modern water temperature at the sea surface (annual mean or summer) and integrated over the upper 200 m water column.

References

Huguet, C., Fietz, S., Rosell-Melé, A., 2013. Global distribution patterns of hydroxy glycerol dialkyl glycerol tetraethers. Organic Geochemistry 57, 107-118.

Ho, S.L., Mollenhauer, G., Fietz, S., Martínez-García, A., Lamy, F., Rueda, G., Schipper, K., Méheust, M., Rosell-Melé, A., Stein, R., Tiedemann, R., 2014. Appraisal of TEX_{86} and TEX_{86}^{L} thermometries in subpolar and polar regions. Geochimica et Cosmochimica Acta 131, 213–226.

Kim, J.H., van der Meer, J., Schouten, S., Helmke, P., Willmott, V., Sangiorgi, F., Koç, N., Hopmans, E.C., Sinninghe Damsté, J.S., 2010. New indices and calibrations derived from the distribution of crenarchaeal isoprenoid tetraether lipids: implications for past sea surface temperature reconstructions. Geochimica et Cosmochimica Acta 74, 4639–4654.

Liu, X.-L., Lipp, J.S., Simpson, J.H., Lin, Y.-S., Summons, R.E., Hinrichs, K.-U., 2012. Mono and dihydroxyl glycerol dibiphytanyl glycerol tetraethers in marine sediments: identification of both core and intact polar lipid forms. Geochimica et Cosmochimica Acta 89, 102–115.

Locarnini, R.A., Mishonov, A.V., Antonov, J.I., Boyer, T.P., Garcia, H.E., Baranova, O.K., Zweng, M.M., Johnson, D.R., 2010. World Ocean Atlas 2009, Volume 1: Temperature. In: Levitus, S. (Ed.), NOAA Atlas NESDIS 68, U.S. Government Printing Office, Washington, D.C., 184 pp.

Martínez-García, A., Rosell-Melé, A., Geibert, W., Gersonde, R., Masqué, P., Gaspari, V., Barbante, C., 2009. Links between iron supply, marine productivity, sea surface temperatures and CO2 over the last 1.1My. Paleoceanography 24, PA1207.

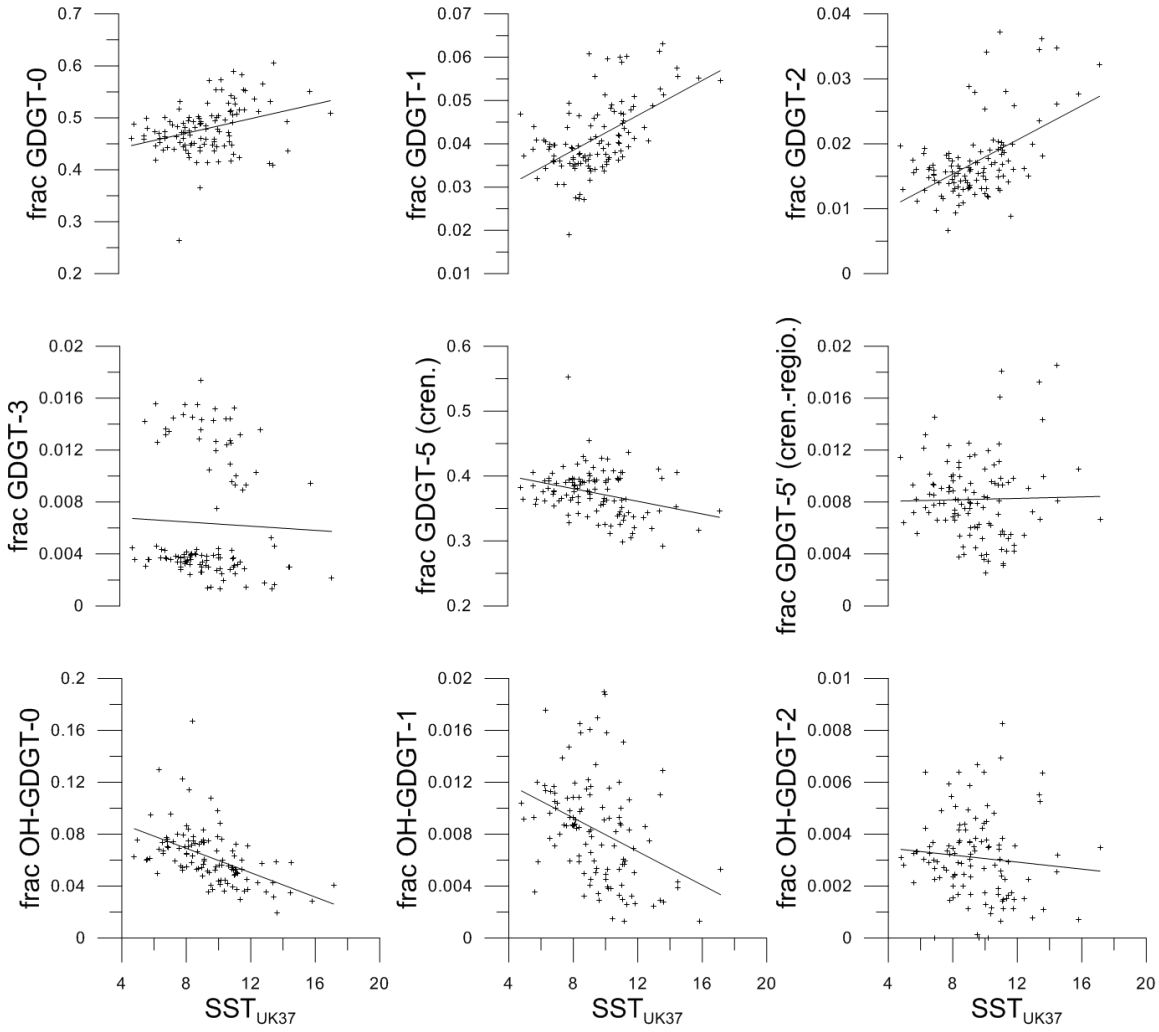

Figure S1A. GDGT fractional abundances (frac; out of total pool of isoprenoidal GDGTs) vs. SST_{UK37} (data from Martínez-García et al., 2009) from PS2489-2 record. Regression statistics (i.e. r and p values) are given in main article Table 1A.

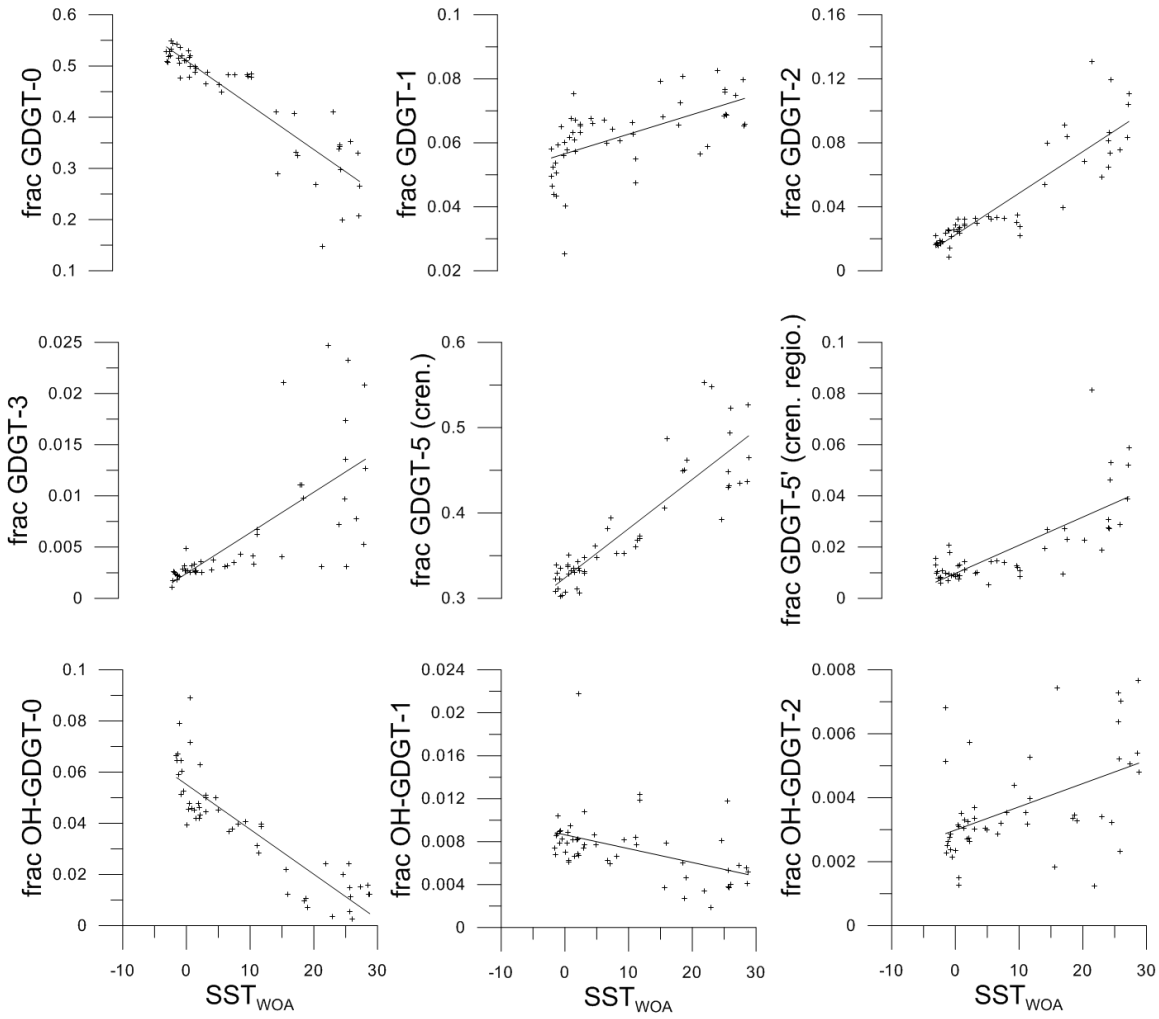

Figure S1B. GDGT fractional abundances (frac; out of total pool of isoprenoidal GDGTs) vs. SST (°C) extracted from World Ocean Atlas 09 (SST_{WOA}; Locarnini et al., 2010). Correlation statistics (i.e., r and p values) are given in main article Table 1B.

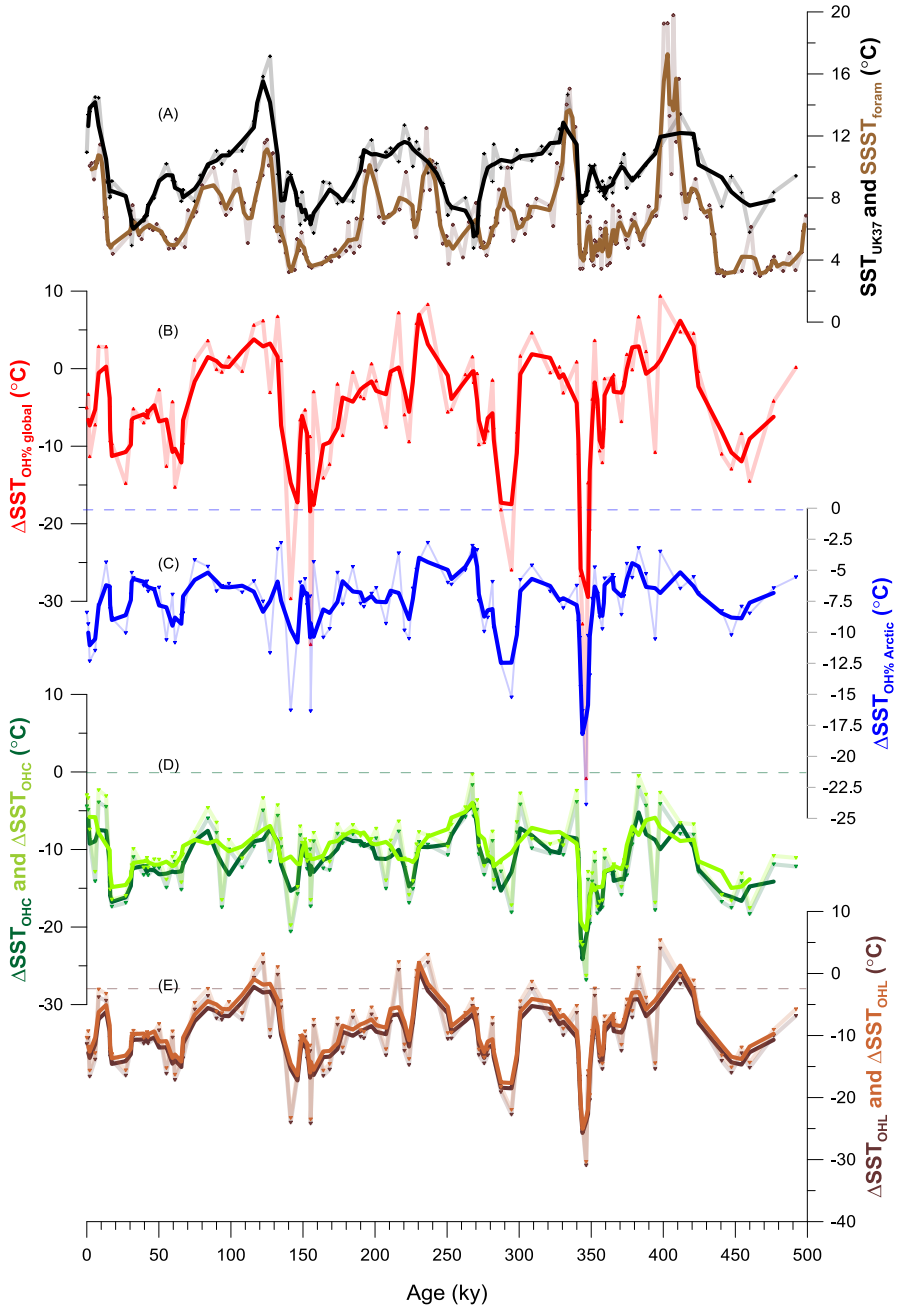

Figure S2. Difference between the modelled temperature based on OH-GDGT indices and SST$_{UK37}$ (ΔSST (°C) = SST$_{OH\%}$ - SST$_{UK37}$). The OH-GDGT based temperatures were calculated using (B) global calibration (Huguet et al., 2013) or (C) Arctic calibration (Fietz et al., 2013). Negative ΔSST (°C) indicate underestimation of SST using OH-GDGTs, while positive ΔSST (°C) indicate overestimation of SST using OH-GDGT. The ΔSST for newly proposed SST$_{OHC}$ and SST$_{OHL}$ are also shown (panels D and E). Thicker curves denote three point running averages. The SST$_{OH\%\ global}$ almost consistently underestimates SST$_{UK37}$ during glacial periods, and overestimates most of the interglacial warmer SST$_{UK37}$. SST$_{OH\%\ Arctic}$, SST$_{OHC}$ and SST$_{OHL}$ produce lower SST than U^{K}_{37} throughout the 500k yr PS2489-2 record.

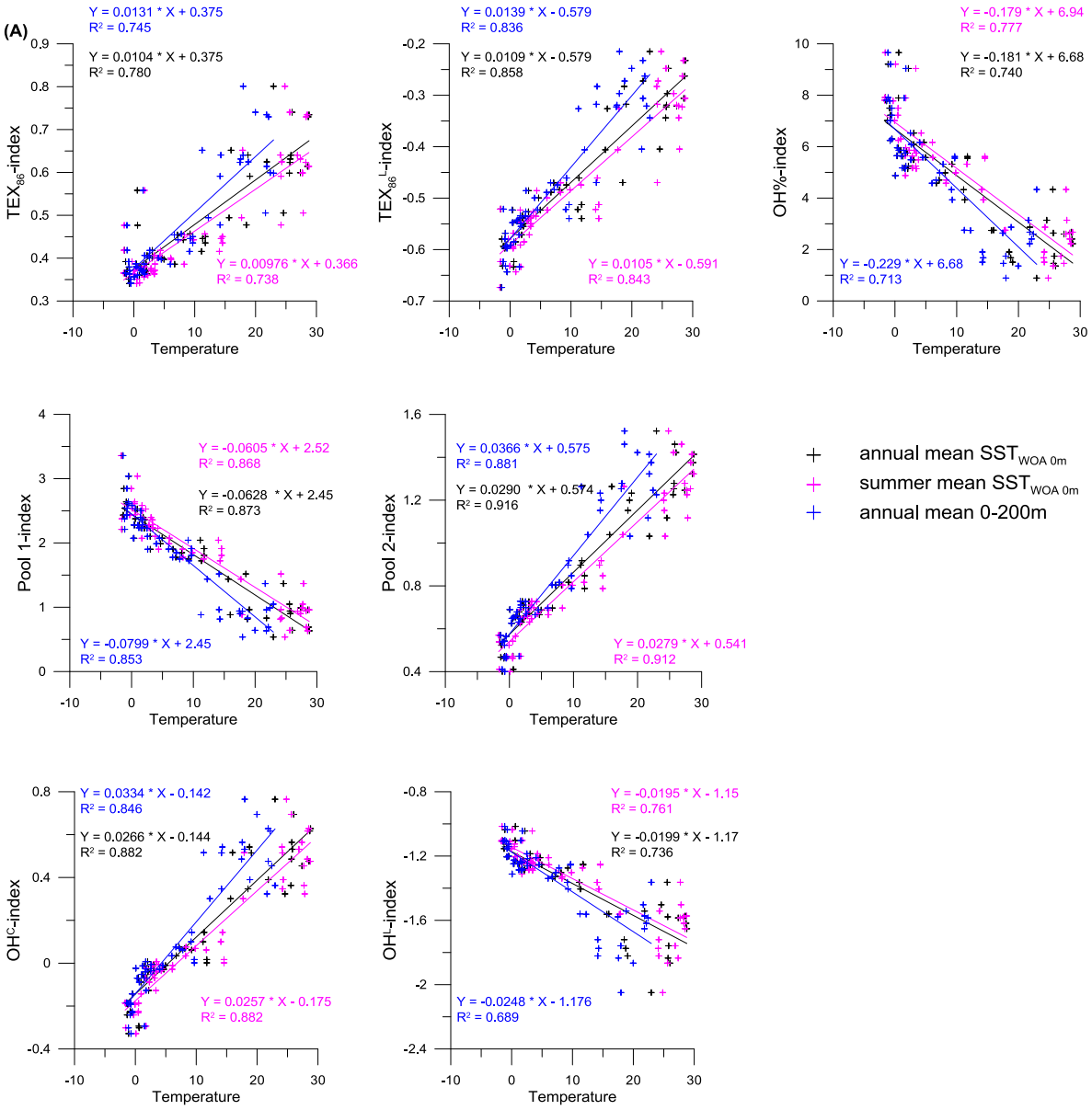

Figure S3. Core-top GDGT indices correlated to water temperature: Correlations between GDGT-indices and atlas water temperatures at core top sites for annual mean at 0 m (black crosses), for summer mean at 0 m (pink crosses) and annual mean integrated over 0-200 m (blue crosses). All temperature data are derived from World Ocean Atlas 09 (Locarnini et al., 2010). Pool 1 and 2 indicate two different GDGT pools, i.e. Pool 1, all TEX_{86} GDGTs and Pool 2, all TEX_{86} GDGTs plus all OH-GDGTs. OH^C and OH^L indicate indices modified with *a priori* observation that relative abundance of OH-GDGTs is related to cold water. The OH^C-index is a modified TEX_{86} index by subtracting the assumed cold water end member OH-GDGT-0 from the numerator. The OH^L-index is the OH% with a log function similar to TEX_{86}^L. Regression statistics (i.e. rse and p values) are given in the main text Table 3.

Table S1. Station coordinates; WOA09 derived annual mean SST, sum of all isoprenoid GDGT (including hydroxyl and non-hydroxylated GDGTs) and fractional abundance of each GDGT. The iso- and OH-GDGT data from tropical-temperate and Arctic core tops as well as some Pacific Southern Ocean core tops were previously used by Huguet et al. (2013). The isoGDGT data from the Pacific Southern Ocean core tops are published by Ho et al. (2014) and most OH-GDGTs are newly added here. To prevent bias on the statistical analysis due to analytical errors associated with samples of low GDGT abundance, we used only samples wherein all nine GDGTs are detected.

sample set	Latitude (°N)	Longitude (°E)	annual mean SST (°C)	summer SST (°C)	0-200m SST (°C)	sum all isoprenoid GDGTs (µg/L)
Arctic	87.070	104.660	0.6	-1.6	-1.13	0.337
Arctic	87.010	-145.710	-1.47	-1.68	-1.38	0.077
Arctic	86.530	152.100	-1.5	-1.6	-1.11	0.142
Arctic	80.500	5.900	0.6	1.8	1.51	4.164
tropic-temperate	40.913	2.079	18.5	24.2	14.16	5.674
tropic-temperate	40.578	3.541	18.8	24.1	14.29	1.612
tropic-temperate	40.133	2.204	19.1	24.2	14.16	1.289
tropic-temperate	32.830	-119.980	16.0	17.9	11.23	0.129
tropic-temperate	31.670	-75.420	24.6	27.8	21.63	13.066
tropic-temperate	27.714	34.682	25.6	27.7	22.96	0.134
tropic-temperate	18.077	-21.026	23.0	24.8	17.97	0.059
tropic-temperate	6.158	112.213	28.5	28.8	21.83	0.132
tropic-temperate	5.383	90.350	28.7	28.3	22.13	1.016
tropic-temperate	4.933	73.283	28.8	28.5	21.82	0.141
tropic-temperate	1.300	-133.600	26.0	25.6	19.98	1.681
tropic-temperate	-1.198	-11.879	25.7	27.4	17.56	2.114
tropic-temperate	-3.667	-37.717	27.4	27.7	22.42	0.216
tropic-temperate	-5.180	10.436	25.7	28.3	17.46	2.895
tropic-temperate	-5.778	-10.750	25.8	26.9	17.95	0.023
tropic-temperate	-29.920	-35.660	21.9	24.3	18.82	0.251
tropic-temperate	-32.591	-73.652	15.7	17.7	12.24	0.279
Pacific SO	-45.758	177.149	11.31	14.33	9.28	0.266
Pacific SO	-59.700	-171.358	3.03	4.38	2.62	0.494
Pacific SO	-60.769	-115.980	3.01	3.81	2.57	0.575
Pacific SO	-61.050	-159.587	0.39	1.66	0.30	1.386
Pacific SO	-68.730	-164.801	-1.35	-0.30	-0.84	0.496
Pacific SO	-44.409	174.625	11.74	14.57	9.69	0.844
Pacific SO	-44.769	174.526	11.74	14.57	9.69	1.026
Pacific SO	-45.806	175.876	11.12	14.05	9.15	0.378
Pacific SO	-48.262	177.273	9.24	11.66	7.79	1.871
Pacific SO	-52.812	-107.805	7.16	8.32	6.66	0.456
Pacific SO	-52.966	-179.010	8.13	9.84	7.26	0.569
Pacific SO	-54.369	-80.090	6.71	8.27	6.00	0.661
Pacific SO	-55.529	-156.140	4.68	6.06	4.02	0.272
Pacific SO	-56.245	-152.655	3.04	4.25	2.51	0.534
Pacific SO	-57.020	-174.430	4.95	6.13	4.51	0.935
Pacific SO	-57.560	-151.219	1.89	3.15	1.46	2.059
Pacific SO	-58.177	-157.637	2.08	3.45	1.65	2.430
Pacific SO	-58.277	-135.626	2.18	3.38	1.77	1.074
Pacific SO	-58.581	-150.066	0.92	2.30	0.63	1.731
Pacific SO	-58.904	-135.621	2.18	3.38	1.77	1.342
Pacific SO	-59.042	-158.364	1.52	2.84	1.18	2.026
Pacific SO	-60.667	-169.502	2.02	3.47	1.69	1.640
Pacific SO	-61.822	-169.741	1.27	2.82	1.04	1.175
Pacific SO	-61.939	-160.119	0.49	1.74	0.37	2.796
Pacific SO	-62.205	-145.619	-0.47	0.94	-0.53	1.121
Pacific SO	-63.694	-169.075	0.06	1.69	0.09	2.087
Pacific SO	-64.744	-161.904	-0.73	0.47	-0.50	0.381
Pacific SO	-64.933	-144.115	-0.79	0.54	-0.77	0.174
Pacific SO	-65.411	-166.155	-0.86	0.50	-0.52	0.677
Pacific SO	-66.788	-163.325	-1.11	0.10	-0.72	0.476
Pacific SO	-67.083	-165.542	-1.24	-0.05	-0.75	0.348

[continued on next page]

[continued]

fractional abundance									
GDGT-0	GDGT-1	GDGT-2	GDGT-3	GDGT-5 (cren.)	GDGT-5' (cren. regio.)	OH-GDGT-1	OH-GDGT-2	OH-GDGT-3	OH-GDGTs and/or isoGDGTs previously published
0.4757	0.0402	0.0141	0.0049	0.3508	0.0177	0.0889	0.0062	0.0015	Huguet et al., 2013
0.5085	0.0579	0.0161	0.0017	0.3221	0.0156	0.0645	0.0068	0.0068	Huguet et al., 2013
0.5276	0.0495	0.0218	0.0010	0.3081	0.0128	0.0666	0.0074	0.0051	Huguet et al., 2013
0.5358	0.0252	0.0084	0.0027	0.3283	0.0207	0.0716	0.0061	0.0013	Huguet et al., 2013
0.4070	0.0654	0.0392	0.0111	0.4488	0.0095	0.0097	0.0060	0.0034	Huguet et al., 2013
0.3311	0.0725	0.0911	0.0111	0.4503	0.0271	0.0107	0.0027	0.0035	Huguet et al., 2013
0.3255	0.0806	0.0840	0.0098	0.4622	0.0229	0.0072	0.0046	0.0033	Huguet et al., 2013
0.2893	0.0682	0.0798	0.0210	0.4873	0.0269	0.0123	0.0078	0.0074	Huguet et al., 2013
0.4101	0.0824	0.0583	0.0072	0.3918	0.0189	0.0201	0.0081	0.0032	Huguet et al., 2013
0.3379	0.0684	0.0647	0.0097	0.4484	0.0276	0.0243	0.0118	0.0073	Huguet et al., 2013
0.1477	0.0588	0.1305	0.0247	0.5479	0.0815	0.0037	0.0019	0.0034	Huguet et al., 2013
0.3298	0.0798	0.0831	0.0052	0.4367	0.0386	0.0159	0.0055	0.0054	Huguet et al., 2013
0.2071	0.0653	0.1037	0.0208	0.5269	0.0521	0.0124	0.0041	0.0077	Huguet et al., 2013
0.2648	0.0658	0.1108	0.0126	0.4649	0.0587	0.0124	0.0051	0.0048	Huguet et al., 2013
0.1995	0.0685	0.1195	0.0232	0.5227	0.0530	0.0026	0.0040	0.0070	Huguet et al., 2013
0.3461	0.0765	0.0865	0.0173	0.4318	0.0272	0.0056	0.0038	0.0052	Huguet et al., 2013
0.3520	0.0749	0.0756	0.0077	0.4351	0.0287	0.0152	0.0057	0.0051	Huguet et al., 2013
0.3429	0.0757	0.0811	0.0135	0.4295	0.0308	0.0148	0.0053	0.0064	Huguet et al., 2013
0.2973	0.0689	0.0736	0.0031	0.4935	0.0461	0.0114	0.0037	0.0023	Huguet et al., 2013
0.2683	0.0564	0.0683	0.0031	0.5527	0.0225	0.0241	0.0034	0.0012	Huguet et al., 2013
0.4096	0.0793	0.0539	0.0041	0.4061	0.0196	0.0219	0.0037	0.0018	Huguet et al., 2013
0.4795	0.0628	0.0350	0.0034	0.3679	0.0122	0.0285	0.0077	0.0032	Huguet et al., 2013; Ho et al., 2014
0.4990	0.0632	0.0320	0.0026	0.3313	0.0109	0.0498	0.0077	0.0034	Huguet et al., 2013; Ho et al., 2014
0.4881	0.0654	0.0292	0.0036	0.3479	0.0109	0.0445	0.0074	0.0030	Huguet et al., 2013; Ho et al., 2014
0.5155	0.0559	0.0253	0.0032	0.3368	0.0068	0.0455	0.0079	0.0031	Huguet et al., 2013; Ho et al., 2014
0.5070	0.0463	0.0175	0.0026	0.3391	0.0098	0.0670	0.0086	0.0023	Huguet et al., 2013; Ho et al., 2014
0.4844	0.0474	0.0218	0.0063	0.3731	0.0108	0.0386	0.0124	0.0053	Ho et al., 2014
0.4771	0.0550	0.0274	0.0067	0.3699	0.0083	0.0398	0.0118	0.0040	Ho et al., 2014
0.4827	0.0662	0.0303	0.0042	0.3606	0.0127	0.0314	0.0084	0.0035	Ho et al., 2014
0.4833	0.0605	0.0327	0.0043	0.3521	0.0139	0.0407	0.0082	0.0044	Ho et al., 2014
0.4495	0.0597	0.0322	0.0032	0.3939	0.0144	0.0379	0.0059	0.0032	Ho et al., 2014
0.4821	0.0643	0.0332	0.0035	0.3527	0.0145	0.0397	0.0067	0.0035	Ho et al., 2014
0.4638	0.0670	0.0337	0.0031	0.3812	0.0054	0.0367	0.0062	0.0029	Ho et al., 2014
0.4649	0.0675	0.0326	0.0027	0.3608	0.0098	0.0500	0.0086	0.0030	Ho et al., 2014
0.4950	0.0657	0.0281	0.0025	0.3292	0.0142	0.0509	0.0107	0.0037	Ho et al., 2014
0.4872	0.0660	0.0299	0.0037	0.3475	0.0099	0.0452	0.0077	0.0030	Ho et al., 2014
0.5300	0.0633	0.0244	0.0033	0.3113	0.0091	0.0477	0.0081	0.0027	Ho et al., 2014
0.5169	0.0608	0.0258	0.0026	0.3349	0.0076	0.0419	0.0068	0.0027	Ho et al., 2014
0.4986	0.0669	0.0269	0.0026	0.3058	0.0087	0.0629	0.0218	0.0057	Ho et al., 2014
0.5193	0.0578	0.0212	0.0026	0.3317	0.0087	0.0457	0.0094	0.0035	Ho et al., 2014
0.5192	0.0572	0.0235	0.0026	0.3319	0.0130	0.0431	0.0067	0.0026	Ho et al., 2014
0.5109	0.0675	0.0284	0.0032	0.3299	0.0083	0.0418	0.0066	0.0033	Ho et al., 2014
0.4774	0.0753	0.0322	0.0027	0.3424	0.0126	0.0460	0.0083	0.0032	Ho et al., 2014
0.5101	0.0616	0.0256	0.0025	0.3348	0.0091	0.0452	0.0081	0.0030	Ho et al., 2014
0.5051	0.0600	0.0248	0.0027	0.3385	0.0093	0.0477	0.0088	0.0031	Ho et al., 2014
0.5441	0.0592	0.0180	0.0021	0.3029	0.0106	0.0527	0.0082	0.0022	Ho et al., 2014
0.5429	0.0650	0.0234	0.0028	0.3073	0.0098	0.0395	0.0070	0.0023	Ho et al., 2014
0.5488	0.0505	0.0180	0.0022	0.3023	0.0060	0.0604	0.0090	0.0029	Ho et al., 2014
0.5327	0.0433	0.0167	0.0018	0.3350	0.0080	0.0512	0.0089	0.0024	Ho et al., 2014
0.5204	0.0535	0.0189	0.0023	0.3222	0.0078	0.0644	0.0079	0.0028	Ho et al., 2014
0.5274	0.0439	0.0159	0.0024	0.3106	0.0077	0.0791	0.0104	0.0026	Ho et al., 2014
0.5185	0.0523	0.0167	0.0026	0.3292	0.0106	0.0590	0.0087	0.0025	Ho et al., 2014

Table S2: Alternative OH-GDGT indices and calibrations applied in Fig. 6 (main manuscript). Numbers for nominator and denominator refer to 0 – GDGT-0 (*m/z* 1302, caldarchaeol), 1 – GDGT-1 (*m/z* 1300), 2 – GDGT-2 (*m/z* 1298), 3 – GDGT-3 (*m/z* 1296), 5 – GDGT-5 (*m/z* 1292, crenarchaeol), 5'– GDGT-5' (*m/z* 1292, crenarchaeol regioisomer), 0* – OH-GDGT-0 (*m/z* 1318), 1* – OH-GDGT-1 (*m/z* 1316), 2* – OH-GDGT-2 (*m/z* 1314). For all regressions we refer the reader to Fig. S3 for the plots and Table 3 (main manuscript) for statistics. See table S2 for more details on Pool 1 and Pool 2 best indices.

Eq.	Regression	R^2
4	$SST_{\%OH\ new} = (\%OH - 6.68)/(-0.181)$	0.74
Description: Regression of %OH vs. atlas SST in the newly compiled core top data set		
5	Pool 1 best index = $-0.0628 \times SST_{WOA} + 2.45$	0.87
Description: Pool 1 best index = (1 + 3)/(2 + 3).		
6	Pool 2 best index = $0.0290 \times SST_{WOA} + 0.574$	0.92
Description: Pool 2 best index = (2 + 3 + 5' + 1*+ 2*) /(2 + 3+ 0*)		
7	$OH^L = -0.0199 \times SST_{WOA} - 1.17$	0.74
Description: OH^L index = $\log_{10}[(\Sigma OHGDGT)/(\Sigma isoGDGT+\Sigma OHGDGT)]$		
8	$OH^C = 0.0266 \times SST_{WOA} - 0.144$	0.88
Description: OH^C index = (2 + 3 + 5' - 0*) /(1 + 2 + 3 + 5' + ΣOHGDGT)		

Table S3. Correlation of GDGT combinations with WOA09-SST (Locarnini et al., 2010) for two pools of GDGTs. All correlations reported here have p values < 0.001. Numbers for nominator and denominator refer to 0 – GDGT-0 (*m/z* 1302, caldarchaeol), 1 – GDGT-1 (*m/z* 1300), 2 – GDGT-2 (*m/z* 1298), 3 – GDGT-3 (*m/z* 1296), 5 – GDGT-5 (*m/z* 1292, crenarchaeol), 5'– GDGT-5' (*m/z* 1292, crenarchaeol regioisomer), 0* – OH-GDGT-0 (*m/z* 1318), 1* – OH-GDGT-1 (*m/z* 1316), 2* – OH-GDGT-2 (*m/z* 1314).
The combinations of the two GDGT pools are defined as:
(a) Pool 1 (210 combinations), consisting of all TEX_{86} GDGTs, i.e. GDGT-1, GDGT-2, GDGT-3 and crenarchaeol regioisomer.
(b) Pool 2 (16002 combinations), consisting of all TEX_{86} GDGTs and all OH-GDGTs, i.e. GDGT-1, GDGT-2, GDGT-3, crenarchaeol regioisomer, OH-GDGT-0, OH-GDGT-1 and OH-GDGT-2.

Pool 1

Rank	r^2	Numerator	Denominator
1	0.873	1+3	2+3
2	0.872	1+2+3	2+3
3	0.872	1	2+3
4	0.866	1+3+5'	2+3+5'
5	0.866	1+5'	2+3+5'

Pool 2

Rank	r^2	Numerator	Denominator
1	0.916	2+3+5'+1*+2*	2+3+0*
2	0.915	2+3+5'+1*	2+3+0*
3	0.912	2+3+4'+1*+2*	2+3+0*+2*
4	0.911	2+3+5'+2*	2+3+0*
5	0.910	5'+1*+2*	3+5'+0*